Tectonophysics 530–531 (2012) 152–179

Contents lists available at SciVerse ScienceDirect

Tectonophysics

journal homepage: www.elsevier.com/locate/tecto

Spatially constant slip rate along the southern segment of the Karakorum fault since 200 ka

Marie-Luce Chevalier [a,b,*], Paul Tapponnier [c], Jérôme Van der Woerd [d], Frederick J. Ryerson [e], Robert C. Finkel [f], Haibing Li [a]

[a] State Key Laboratory for Continental Tectonics and Dynamics, Institute of Geology, CAGS, 26 Baiwanzhuang St, Beijing 100037, China
[b] Laboratoire de Tectonique et Mécanique de la lithosphère, Institut de Physique du Globe de Paris, 4, Place Jussieu, 75252 Paris cedex 05, France
[c] Earth Observatory of Singapore, 50 Nanyang Ave, N2-01a-09, Singapore 639798, Singapore
[d] Institut de Physique du Globe de Strasbourg, UMR 7516 CNRS/Université de Strasbourg, 5 rue Descartes, 67084 Strasbourg, France
[e] L-231, Atmospheric, Earth and Energy Division, Physical and Life Sciences Directorate, Lawrence Livermore National Laboratory, Livermore, CA 94550, USA
[f] Earth and Planetary Science Department, University of California, Berkeley, 371 McCone Hall, Berkeley, CA 94720, USA

ARTICLE INFO

Article history:
Received 24 June 2011
Received in revised form 6 December 2011
Accepted 9 December 2011
Available online 23 December 2011

Keywords:
Active tectonics
Tectonic-geomorphology
Slip-rate
Karakorum fault
Tibet
Cosmogenic dating

ABSTRACT

Determining the slip-rate history along the right-lateral Karakorum fault (KF) is fundamental to understanding its present-day kinematic role in the deformation of Tibet. Geodetic and geologic studies suggest slip-rates of 0–11 mm/yr along this structure. Whether slip-rate variability exists along strike and/or time, or simply results from different measuring techniques/timescales, remains unknown. In order to constrain slip-rates within a timescale of 200 ka, we studied fluvial and glacial geomorphic features that are right-laterally or vertically offset by the fault by varying amounts from 7 ± 1 m to 430 ± 30 m and up to 53 ± 5 m, respectively. We constrained their ages using ^{10}Be surface exposure dating on 141 quartz-rich samples collected on 4 lateral moraines and at 3 alluvial sites along the southernmost segment of the KF (Menshi–Kailas basin) and along the Gurla Mandhata detachment fault in the Pulan graben. From the 30° fault bend at Baer (80.5°E) to Mount Kailas area, the slip-rate along the KF is $>7.1^{+3.2}/_{-1.7}$ mm/yr at Menshi and $>7.9^{+3.2}/_{-2.5}$ mm/yr at Kailas (slip on two parallel fault strands). In the Pulan graben, the normal fault slip-rate is $>1.6^{+0.4}/_{-0.3}$ mm/yr. Our data suggest that the Quaternary slip-rate along the southern KF does not decrease eastward but is constant along strike for at least 200 km, from >5–11 mm/yr in the Gar basin further north to >7–8 mm/yr in the Menshi–Kailas basin. Because no expected along-strike slip-rate gradient is observed, it implies that the KF does not end at the Kailas but must extend where the slip rate decreases, i.e. eastward along the Yarlung Zangbo suture and southward along the Gurla Mandhata–Humla fault system.

1. Introduction

Slip-rates on the major strike-slip faults of the Tibetan Plateau (inset, Fig. 1) have been the target of detailed studies in the past decade. Using ^{14}C or cosmogenic nuclides (^{10}Be, ^{26}Al) dating techniques, an increasing number of late Pleistocene/Holocene geological slip-rates have been determined from offset geomorphic features, such as glacial moraines (e.g. Brown et al., 2002; Chevalier et al., 2005a; Harkins et al., 2010; Lasserre et al., 2002; Meriaux et al., 2004), fluvial fans (e.g. Brown et al., 2002; Gold et al., 2011; Meriaux et al., 2005; Van der Woerd et al., 1998, 2000, 2002) and terraces (e.g. Chevalier et al., 2011b; Cowgill et al., 2009; Gold et al., 2009, 2011; Harkins and Kirby, 2008; Harkins et al., 2010; Kirby et al., 2007; Lasserre et al., 1999; Li et al., 2005; Meriaux et al., 2004, 2005; Van der Woerd et al., 1998, 2000, 2002). Geodetic techniques, such as GPS and InSAR (e.g. Bendick et al., 2000; Chen et al., 2000, 2004; Jolivet et al., 2008; Wallace et al., 2004; Wang et al., 2001; Wright et al., 2004; Zhang et al., 2004) yield short timescale slip-rates (10–20 yrs). On certain faults (e.g. Altyn Tagh), the discrepancy between geodetic and geologic slip-rates is a subject of debate (e.g. Cowgill, 2007; Cowgill et al., 2009; Hanks and Thatcher, 2006; Ryerson et al., 2006; Thatcher, 2007).

The slip-rate on the >1000 km-long right-lateral Karakorum fault (Fig. 1), north of the western Himalayan and Karakorum Ranges, is also debated. At the decadal timescale, InSAR observations suggest a rate of 1 ± 3 mm/yr (Wright et al., 2004), while GPS data yield estimates of ~3–4 mm/yr (Chen et al., 2004; Jade et al., 2004, 2010) to 11 ± 4 mm/yr (Banerjee and Burgmann, 2002). At the late Pleistocene timescale, Liu (1993) inferred a geologic slip-rate of ~30 mm/yr, by correlating the emplacement of offset moraines or alluvial fans mapped from 10 m-resolution SPOT satellite images with cold or warm climatic epochs, respectively. On one branch of the fault

* Corresponding author at: State Key Laboratory for Continental Tectonics and Dynamics, Institute of Geology, CAGS, 26 Baiwanzhuang St, Beijing 100037, China. Tel.: +86 13466654223.
E-mail addresses: mlchevalier@hotmail.com (M.-L. Chevalier), tappon@ntu.edu.sg (P. Tapponnier), jeromev@unistra.fr (J. Van der Woerd), ryerson1@llnl.gov (F.J. Ryerson), rfinkel@berkeley.edu (R.C. Finkel), lihaibing06@yahoo.com.cn (H. Li).

0040-1951/$ – see front matter © 2011 Elsevier B.V. All rights reserved.
doi:10.1016/j.tecto.2011.12.014

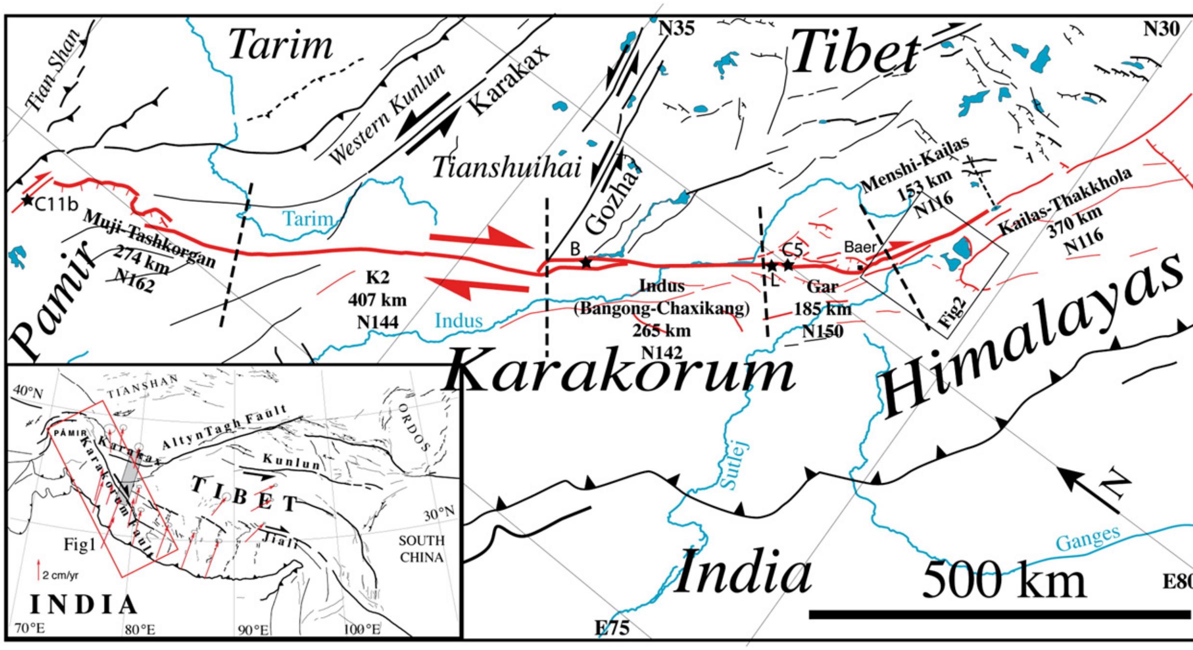

Fig. 1. Large-scale segmentation of the Karakorum fault (KF). First-order geometrical segmentation based on sharp bends and fault junctions divide the KF into six segments with lengths ranging from 150 to 407 km. The Menshi–Kailas segment presented in this paper strikes N116°E and is linked to the average N145°E striking central segments of the KF through a sharp 30° bend at Baer within the Gar segment. Black stars show location of other studies: B = Brown et al. (2002), L = Lacassin et al. (2004), C5 = Chevalier et al. (2005a, 2005b), C11b = Chevalier et al. (2011b). Inset map shows location of the KF within the Tibetan Plateau and Asia. Red arrows show a subset of representative GPS velocities relative to Siberia (Wang et al., 2001; Zhang et al., 2004). The shaded rectangle shows the position of the InSAR swath used by Wright et al. (2004).

north of Bangong Lake in India, Brown et al. (2002) obtained a Holocene slip-rate of 4 ± 1 mm/yr from ^{10}Be cosmic-ray surface exposure dating of a debris flow. Using the same technique on large, well-defined moraines on another single branch of the fault on the west side of the Gar pull-apart basin, Chevalier et al. (2005a, 2005b) determined a late Pleistocene slip-rate of $>5.5 \pm 0.5$ to $>10.7 \pm 0.7$ mm/yr. At the northernmost tip of the KF, along the Muji–Tashkorgan segment, Chevalier et al. (2011b) recently determined, based on offset terraces, a minimum Holocene slip-rate of 4.5 mm/yr along one single branch of the fault (the Muji fault), or >9 mm/yr across the KF system. From joint inversions of geologic and geodetic observations, Loveless and Meade (2011) recently suggested, making the assumption that time variation in fault slip-rates from decadal to Quaternary scales is negligible (using a microplate rotation model), that the segment south of Bangong Lake was moving at a rate of 3.0 ± 0.1 to 5.4 ± 0.3 mm/yr. They note however that if the model assumes larger blocks in central Tibet, this rate could be up to ~8 mm/yr.

Like the Altyn Tagh fault (e.g. Meriaux et al., 2004, 2005; Peltzer et al., 1989), the Karakorum "fault" is a rather complex fault system that splays and joins at places, with several adjacent active or recent faults onto which slip is transferred. For example the KF meets with the Altyn Tagh–Karakax fault south of the Paghman basin, with the Gozha fault north of Bangong Lake, and with one branch of the Karakorum–Jiali fault zone near Chaxikang (Fig. 1 and inset). This contrasts with the Kunlun fault, another major Asian fault with a relatively simple geometry and constant slip-rate along strike (e.g. Harkins and Kirby, 2008; Harkins et al., 2010; Van der Woerd et al., 1998, 2000, 2002). This study aims at better understanding if the KF slip-rate behaves like that of the Altyn Tagh fault (not constant along strike, decreasing away from the central segment, e.g. Meriaux et al., 2005; Meyer et al., 1996; Zhang et al., 2007) or like that of the Kunlun fault.

In this paper, we add quantitative geomorphologic and chronologic data along the southernmost, Menshi–Kailas segment of the Karakorum fault (Figs. 1 and 2). By measuring geomorphic offsets across two branches of the Karakorum fault (Kailas Range Front and Darchen faults) and constraining the offset ages with ^{10}Be cosmic-ray surface exposure dating of fluvial and glacial surfaces, we determine the slip-rate across the two main active branches of the Karakorum fault (KF) system at longitude ~81°E.

This new evidence improves our understanding of the macro-tectonics of Central Asia because slow rates have been argued to favor continuous deformation models (e.g. Bendick et al., 2000; England and Molnar, 1997, 2005) while fast rates argue in favor of block models (e.g. Armijo et al., 1989; Avouac and Tapponnier, 1993; Peltzer and Tapponnier, 1988; Tapponnier et al., 2001). As discussed in recent papers (e.g. Flesch and Bendick, 2007; Loveless and Meade, 2011; Meade, 2007a,b; Thatcher, 2007, 2009), existing velocity fields and geologic rates on active faults in Asia are still too sparse and poorly constrained, both spatially and temporally, to discriminate between a wide range of mechanical conditions. Thus, new slip-rate data at different timescales and locations are warranted to determine whether the discrepancy between geodetic and geologic rates is real, as well as to better understand deformation in this region.

2. Regional active tectonics

The Menshi–Kailas segment, ~160 km-long, is the southernmost segment of the KF system, and borders the southern Kailas Range (Figs. 1 and 2). It strikes on average N116°E, north/south of a ~30° bend in the N150°E striking Gar segment near the village of Baer at the western terminus of the Ayilari Range (~80.5°E, Fig. 1). The Menshi basin marks the drainage divide between the Indus-Gar and Sutlej catchments (Fig. 1).

In Fig. 2, we present detailed mapping of fault strands that offset Quaternary moraines, alluvial fans and terraces. The geometry of the KF south of the Kailas Range is particularly complex, characterized by splaying into multiple branches (Armijo et al., 1989; Lacassin et al., 2004; Murphy and Burgess, 2006; Murphy and Copeland, 2005; Valli et al., 2007). In general, faulting is characterized by strike-slip and thrust faulting that is partitioned along different fault branches. Strike-slip faulting mostly characterizes the right-stepping fault segments across the middle of the basin, separated by pull-aparts or normal faults.

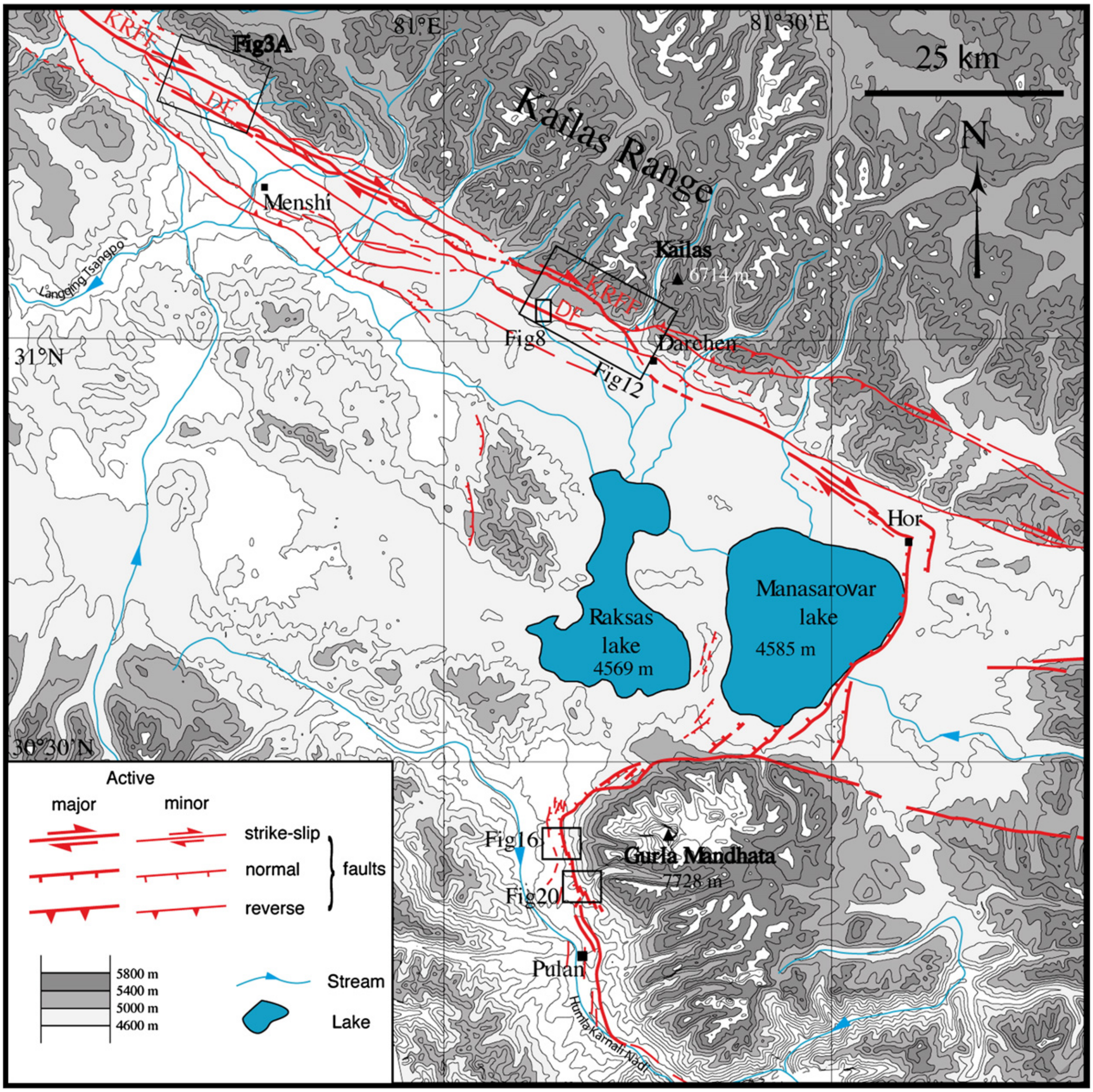

Fig. 2. Faults map of the Menshi–Kailas segment of the KF and associated Pulan half-graben. KRFF = Kailas Range Front fault, DF = Darchen fault. Right-lateral movement is distributed over several sub-parallel strands, which connect through pull-aparts or transfer faults. At Hor, right-lateral slip is partly transferred to the ~NS normal faults along the eastern shore of Lake Manasarovar, which further connects to the Pulan half-graben. Extension south of Hor may explain the origin of the lakes. Boxes indicate location of the study sites where fault strands cut either alluvial terraces or moraine ridges.

Thrust faulting is dominantly localized along the steep range-front fault (the Kailas Range Front Fault or KRFF) (e.g. Lacassin et al., 2004) and along northward shallow dipping thrusts marked by cumulative scarps across alluvial terraces southeast of Menshi (Fig. 2).

The two most active fault strands lie north of the Raksas and Manasarovar Lakes (Fig. 2). One strand, with both strike-slip and normal components, the latter increasing eastward, follows the front of the Kailas Range (KRFF) at the base of triangular facets that separate large glacial valleys (Fig. 2). The other dominantly strike-slip strand strikes parallel to the range-front fault, about 5 km to the south, within the basin. We refer to this fault strand, which meets the KRFF near Darchen (Fig. 2), as the Darchen fault (DF). Other active strands, which we did not investigate in detail, cut through swamps and active fans farther south (Fig. 2). We infer that they also contribute to a small fraction of the KF system's slip-rate. One branch of the fault splays southward around the eastern shore of Lake Manasarovar (Figs. 1 and 2), where its slip component becomes predominantly normal, and continues southwestward into the Pulan graben, along the base of the Gurla Mandhata gneiss dome (Armijo et al., 1989; Lacassin et al., 2004). It has been suggested, based on similar timing constraints, kinematics, and slip estimates for both the KF and the Gurla Mandhata detachment fault (Murphy et al., 2002), that the Pulan rift marks the eastern termination of the KF (with the Gurla Mandhata being a topographic anomaly at the southern tip of the KF, identical to the Mustagh Ata topographic anomaly at its northern tip in the Pamir, Arnaud et al., 1993; Ratschbacher et al., 1994). However, others document evidence that the Karakorum fault zone continues east of 81°30′E (Chen et al., 2004, based on a GPS numerical model; Lacassin et al., 2004, based on the outcrop scale deformation and the regional geometry), reactivating the Yarlung–Zangbo suture (Peltzer and Tapponnier, 1988). At an even greater scale, it has been proposed that the right-lateral component of motion on the KF was transferred either north of the Gangdese Range along the Karakorum–Jiali fault zone (Armijo et al., 1989), or south of the suture into the High Himalaya of Western Nepal (Gurla Mandhata–Humla fault system, Murphy and

Copeland, 2005) then continues as dextral slip along a series of en-echelon faults (including the Humla, Tibrikot, and Bari Gad faults) (Styron et al., 2011).

3. Methods

3.1. Geomorphological analysis

The Menshi–Kailas fault system is located along the southern rim of the Kailas Range, a source of numerous glacial and fluvial valleys flowing southward across the Menshi and Darchen–Hor basins. To the west the drainages feed the upper reach of the Sutlej (Langoing Tsangpo) and to the east the drainages feed the Raksas and Manasarovar Lakes. Most of the abandoned fluvio-glacial terraces and moraines are thus cut mainly orthogonally by the active fault strands of the Menshi–Kailas segment, an optimal situation for documenting the faulting behavior of the different fault stretches.

Fault mapping and geomorphological analysis were performed using different kinds of data, including field observations, topographic data and satellite images. The images used are Landsat 7 images (resolution of 28 m), ASTER images (resolution of 15 m), grayscale SPOT images (resolution of 10 m), grayscale Corona images (resolution of 4 m) and high resolution (1 m) Quickbird images from Geoeye available on GoogleEarth. The images were analyzed together with topographic data from 1/50,000 scale Chinese topographic maps. By combining the different types of observations we were able to map the active fault strands of the Menshi–Kailas segment of the KF, and assess their relative importance and kinematics based on the deformation of surface morphology (Fig. 2). Most of the deposits are alluvial fans, terraces, and moraines. We determined relative ages based on deposit imbrications (carefully checked in the field, together with the satellite images and topographic maps) and relative height above active river-beds. At a more local scale and at targeted sites, surface ages have been assessed using cosmogenic nuclide surface-exposure dating.

3.2. Surface exposure dating

We collected surface and sub-surface samples for ^{10}Be cosmic-ray surface-exposure dating on different alluvial fans, terraces and moraines. Altogether, 141 quartz-rich samples from cobbles (10 to 25 cm in diameter) and boulders (>25 cm in diameter) were collected, 28 (+6 for the depth profile) from Menshi (Site 1), 31 from La Zhi Tang

Table 1
Analytical results of ^{10}Be geochronology at Menshi and surface exposure ages.

Sample name	Lat (N)	Long (E)	Elev (m)	Thickness (cm)	Quartz/granite	Quartz (g)	Be carrier (mg)	$^{10}Be/^{9}Be$ 10^{-15}	^{10}Be (10^6 atom/g)	Standard used[a]	Model 1 LS dep Ages (ka)[b]	Model 2 LS dep Ages (ka)[b,c]
T1												
ZI-100	31,286	80,700	4668	4	g	20.8	0.491	1460 ± 21	2.305 ± 0.033	LLNL3000	27.36 ± 2.36	23.82 ± 2.2
ZI-101	31,286	80,700	4657	4	g	15.17	0.428	1556 ± 37	2.935 ± 0.07	LLNL3000	34.08 ± 3.01	31.68 ± 3.09
ZI-103	31,286	80,699	4662	4	g	14.39	0.409	913 ± 24	1.735 ± 0.046	LLNL3000	21.19 ± 1.88	16.77 ± 1.62
ZI-104	31,286	80,699	4650	7	g	10.03	0.436	1009 ± 25	2.937 ± 0.073	KNSTD	36.28 ± 3.22	34.04 ± 3.35
ZI-105	31,287	80,700	4656	7	g	10.47	0.439	548 ± 16	1.537 ± 0.046	KNSTD	20.26 ± 1.82	15.34 ± 1.52
ZI-106	31,287	80,700	4653	10	g	10.03	0.438	466 ± 12	1.36 ± 0.035	KNSTD	18.5 ± 1.64	13.22 ± 1.28
ZI-107	31,287	80,700	4650	3	q	10.13	0.444	1678 ± 28	4.917 ± 0.084	KNSTD	57.70 ± 5.04	61.14 ± 6.27
ZI-108	31,287	80,700	4653	7	q	10.21	0.443	1850 ± 46	5.367 ± 0.133	KNSTD	65.02 ± 5.81	70.67 ± 7.64
T3S												
ZI-110	31,286	80,700	4667	4	q	15.72	0.407	5809 ± 142	10.065 ± 0.246	LLNL3000	111.09 ± 10.03	151.77 ± 20.84
ZI-111	31,285	80,700	4660	4	q	10.68	0.427	6881 ± 100	18.401 ± 0.268	LLNL3000	205.80 ± 18.54	/
ZI-112	31,285	80,700	4657	4	q	14.32	0.414	2291 ± 61	4.433 ± 0.119	LLNL3000	48.79 ± 4.37	49.98 ± 5.14
ZI-113	31,286	80,700	4660	4	g	15.2	0.412	6643 ± 64	12.034 ± 0.117	LLNL3000	132.25 ± 11.6	210.17 ± 33.87
ZI-114	31,286	80,701	4671	6	g	10.35	0.425	3955 ± 88	10.874 ± 0.242	KNSTD	126.35 ± 11.37	192.64 ± 30.18
ZI-115	31,286	80,701	4676	6	g	10.68	0.446	2977 ± 38	8.318 ± 0.106	KNSTD	98.67 ± 8.62	123.35 ± 15.13
ZI-116	31,286	80,701	4676	7	g	10.12	0.442	3035 ± 63	8.851 ± 0.183	KNSTD	104.98 ± 9.36	137 ± 17.89
ZI-117	31,285	80,701	4671	4	q	9.52	0.431	4300 ± 61	13.017 ± 0.186	KNSTD	150.57 ± 13.37	266.12 ± 51.42
ZI-118	31,285	80,701	4667	4	q	10.97	0.439	1012 ± 24	2.708 ± 0.066	KNSTD	32.87 ± 2.91	29.99 ± 2.91
ZI-119	31,285	80,702	4667	7	g	10.2	0.450	4300 ± 57	12.673 ± 0.168	KNSTD	150.66 ± 13.35	271.29 ± 54.08
T3N												
ZI-120	31,29	80,714	4773	4	g	12.3	0.459	3170 ± 47	7.918 ± 0.119	LLNL3000	84.92 ± 7.43	101.63 ± 11.72
ZI-121	31,29	80,713	4765	8	g	2.68	0.397	1145 ± 19	11.352 ± 0.195	LLNL3000	122.7 ± 10.89	185.31 ± 27.94
ZI-122	31,29	80,714	4785	4	g	15.06	0.449	2580 ± 38	5.149 ± 0.076	LLNL3000	54.21 ± 4.7	57.79 ± 5.85
ZI-123	31,29	80,713	4754	3	g	19.56	0.476	4140 ± 60	6.74 ± 0.099	LLNL3000	71.98 ± 6.27	82.66 ± 9
ZI-124	31,29	80,714	4785	6	g	10.1	0.454	3270 ± 49	9.815 ± 0.147	KNSTD	109.28 ± 9.62	148.64 ± 19.82
ZI-125	31,29	80,713	4752	5	g	9.54	0.444	1995 ± 60	6.203 ± 0.187	KNSTD	70.47 ± 6.42	82.23 ± 9.4
ZI-126	31,29	80,714	4785	7	g	10.03	0.454	2822 ± 67	8.54 ± 0.204	KNSTD	97.31 ± 8.74	121.01 ± 15.19
ZI-127	31,289	80,712	4744	5	g	10.64	0.448	4185 ± 99	11.77 ± 0.278	KNSTD	131.15 ± 11.87	206.54 ± 34.01
ZI-128	31,289	80,712	4744	5	g	10.07	0.423	4155 ± 64	11.679 ± 0.182	KNSTD	130.13 ± 11.52	203.42 ± 32.41
ZI-129	31,288	80,712	4740	6	g	5.86	0.450	1742 ± 27	8.957 ± 0.142	KNSTD	102.53 ± 9.02	131.97 ± 16.74
Depth profile				Depth below surface (cm)								
DP-50	31,264	80,698	4580	50	g	12.33	0.458	513 ± 12	1.273 ± 0.031	KNSTD		
DP-100	31,264	80,698	4580	100	g	12.15	0.446	574 ± 13	1.409 ± 0.034	KNSTD		
DP-150	31,264	80,698	4580	150	g	22.37	0.498	577 ± 23	0.859 ± 0.034	KNSTD		
DP-200	31,264	80,698	4580	200	g	9.99	0.449	443 ± 10	1.333 ± 0.032	KNSTD		
DP-250	31,264	80,698	4580	250	g	26.62	0.752	381 ± 9	0.719 ± 0.017	KNSTD		
DP-300	31,264	80,698	4580	300	g	18.47	0.537	227 ± 6	0.442 ± 0.011	KNSTD		

The ages are calculated with the CRONUS 2.2 (with constants 2.2.1) calculator using the time-dependent Lal (1991)/Stone (2000) production rate model. Shielding factor is 0.99; sample density is 2.7 g/cm^3 for granite and 2.65 g/cm^3 for quartzite.

[a] ^{10}Be isotope ratios for KNSTD = 3.11×10^{-12} and for LLNL3000 = 3×10^{-12}.

[b] External uncertainties (analytical and production rate) are reported at the 1 s confidence level.

[c] We applied an erosion rate of 3×10^{-4} cm/yr and subtracted mean inheritance (concentration of the deepest sample at the nearby depth profile $0.442 \pm 0.011 \times 10^6$ atom/g).

(Site 2), 7 from the A Qu moraine (Site 3), 22 from the West and East Xiong Se moraines (Site 4), 29 from the Rengongpu terraces (Site 5) and 18 from the Rongguo moraines (Site 6). The samples were processed at the Lawrence Livermore National Laboratory (LLNL) and the ^{10}Be/^{9}Be ratios were measured at the Center for Accelerator Mass Spectrometry (CAMS) at LLNL. For more detailed information about the dating technique, we refer the reader to Gosse and Phillips (2001).

Details about the samples (location, thickness, rock type, quartz weight, amount of Be carrier added, ^{10}Be/^{9}Be ratio, ^{10}Be concentration and standard used) are listed in Tables 1–3 for the alluvial terrace sites (Sites 1, 2 and 5) and in Chevalier et al. (2011a) for the moraine sites (Sites 3, 4 and 6). The model ages were calculated with the CRONUS Earth 2.2 calculator (with constant file 2.2.1) (Balco et al., 2008; http://hess.ess.washington.edu/), using the time-dependent Lal (1991)/Stone (2000) production rate model. For information, Table S1 in the Supplemental material shows the ages calculated with the other available production rate models (Desilets and Zreda, 2003; Desilets et al., 2006; Dunai, 2000, 2001; Lifton et al., 2005). Individual model age uncertainties refer to external uncertainties (i.e. analytical and production rate) and are reported at the 1-sigma (s) confidence level (Tables 1–3 and S1). In this paper, we report median ages (for each surface) and slip-rates (Table 4) calculated using the method of Zechar and Frankel (2009), with uncertainties at the 68.27% confidence interval about the median. In Table 4, we report mean and mode ages and slip-rates, as well as uncertainties at the 95.45% confidence interval about the median.

We calculate the ages at the fluvial sites (i.e. Menshi, La Zhi Tang and Rengongpu) with two different assumptions (Tables 1–3). A first set of ages (Model 1) is obtained assuming no erosion and no inheritance in the samples. A second set of ages (Model 2) is obtained by applying an erosion rate and subtracting inheritance. We apply an average erosion rate of 3×10^{-4} cm/yr, even if erosion rates may vary widely from site to site within a given region. This rate is derived from bedrock erosion rates found in the internally-drained part of the Tibetan Plateau (Lal et al., 2003), and considered as maximum possible erosion rates for the terraces since bedrock outcrops are far more subject to erosion compared to flat alluvial surfaces. An average inheritance distributed in all the samples is estimated from present-day river-bed samples (Sites 2 and 5) or from a depth profile (near Site 1).

We carefully selected and sampled surfaces with no sign of fluvial incision, i.e. those most likely to have negligible post-depositional erosion. In particular, we sampled flat surfaces away from post-deposition rills and away from adjacent slopes that may feed alluvial material to the surface during degradation. Nevertheless, chemical weathering, in-situ degradation and wind deflation cannot be ruled

Table 2
Analytical results of ^{10}Be geochronology for the La Zhi Tang site (LZT) and surface exposure ages.

Sample name	Lat (N)	Long (E)	Elev (m)	Thickness (cm)	Quartz/granite	Quartz (g)	Be carrier (mg)	^{10}Be/^{9}Be 10^{-15}	^{10}Be (10^6 atom/g)	Model 1 LS dep Ages (ka)[a]	Model 2 LS dep Ages (ka)[a,b]
T0											
24LQ-T01	31,032	81,13	4866	4	g	20.7074	0.41721	124 ± 5	0.167 ± 0.007		
24LQ-T02	31,032	81,13	4866	4	g	20.4712	0.41438	265 ± 7	0.359 ± 0.01		
24LQ-T03	31,032	81,13	4866	4	g	20.4968	0.40998	466 ± 11	0.624 ± 0.015		
24LQ-T04	31,032	81,13	4866	4	g	21.3837	0.41079	78 ± 2	0.1 ± 0.003		
T1											
ZI-65	31,032	81,129	4886	11	g	10.482	0.40271	541 ± 11	1.389 ± 0.028	16.62 ± 1.45	13.52 ± 1.27
ZI-66	31,032	81,129	4884	4	g	10.4928	0.41640	596 ± 15	1.581 ± 0.041	17.77 ± 1.57	15.03 ± 1.43
ZI-68	31,032	81,129	4884	2	g	10.3537	0.40485	318 ± 8	0.832 ± 0.021	9.4 ± 0.83	6.02 ± 0.62
ZI-69	31,032	81,129	4883	5	g	10.4551	0.42893	333 ± 9	0.914 ± 0.025	10.59 ± 0.94	7.05 ± 0.71
ZI-75	31,033	81,129	4889	4	g	10.259	0.41143	309 ± 8	0.83 ± 0.022	9.52 ± 0.84	6.08 ± 0.63
ZI-76	31,033	81,129	4889	5	q	10.2104	0.41972	401 ± 10	1.103 ± 0.029	12.73 ± 1.12	9.33 ± 0.91
ZI-78	31,033	81,129	4889	8	g	10.1284	0.42755	331 ± 8	0.935 ± 0.025	11.07 ± 0.98	7.45 ± 0.75
ZI-79	31,033	81,129	4890	7	q	10.7371	0.47927	1413 ± 28	4.216 ± 0.086	43.04 ± 3.77	44.54 ± 4.4
T1′											
ZI-60	31,032	81,127	4889	4	g	10.4383	0.40828	370 ± 8	0.968 ± 0.022	11.08 ± 0.97	7.59 ± 0.74
ZI-62	31,032	81,127	4889	4	g	11.9474	0.40465	444 ± 11	1.007 ± 0.025	11.53 ± 1.01	8.06 ± 0.79
ZI-63	31,032	81,128	4887	4	g	10.1873	0.40525	303 ± 8	0.806 ± 0.022	9.23 ± 0.82	5.82 ± 0.61
ZI-64	31,032	81,128	4887	4	g	10.4641	0.41087	1093 ± 26	2.868 ± 0.07	30.52 ± 2.7	29.46 ± 2.84
ZI-70	31,033	81,127	4894	3	q	10.1946	0.42174	345 ± 9	0.956 ± 0.025	10.82 ± 0.96	7.36 ± 0.74
ZI-71	31,033	81,127	4891	4	g	10.2913	0.42380	340 ± 9	0.937 ± 0.024	10.72 ± 0.95	7.23 ± 0.72
ZI-72	31,033	81,127	4891	5	g	10.4339	0.40044	405 ± 10	1.039 ± 0.026	12 ± 1.06	8.52 ± 0.83
ZI-74	31,033	81,128	4891	4	g	10.3748	0.41539	381 ± 9	1.022 ± 0.024	11.69 ± 1.02	8.23 ± 0.8
T1″											
ZI-55	31,032	81,126	4883	4	g	10.3202	0.42396	413 ± 10	1.135 ± 0.029	13.04 ± 1.15	9.69 ± 0.94
ZI-56	31,032	81,126	4891	7	g	10.2019	0.40461	726 ± 15	1.925 ± 0.04	21.77 ± 1.9	19.34 ± 1.81
ZI-57	31,032	81,127	4889	4	g	10.1115	0.41030	418 ± 11	1.135 ± 0.03	13 ± 1.15	9.66 ± 0.94
ZI-58	31,032	81,127	4888	8	g	10.8775	0.41236	376 ± 10	0.952 ± 0.025	11.28 ± 1	7.67 ± 0.77
ZI-59	31,032	81,127	4888	4	g	10.2488	0.40881	388 ± 11	1.034 ± 0.031	11.86 ± 1.06	8.4 ± 0.84
T2											
ZI-50	31,037	81,127	4913	3	g	10.1807	0.40570	1691 ± 39	4.505 ± 0.106	62.49 ± 5.49	70.27 ± 7.47
ZI-51	31,038	81,127	4917	4	g	10.4356	0.42214	1446 ± 28	3.909 ± 0.076	61.76 ± 5.48	69.17 ± 7.41
ZI-53	31,038	81,127	4913	7	g	10.3382	0.43979	1747 ± 27	4.969 ± 0.078	49.01 ± 4.26	53.16 ± 5.34
ZI-80	31,033	81,125	4890	4	g	10.5053	0.41014	2345 ± 46	6.121 ± 0.12	43.96 ± 3.89	46.03 ± 4.62
ZI-83	31,032	81,125	4893	5	g	10.304	0.41608	2225 ± 52	6.005 ± 0.141	39.23 ± 3.42	39.91 ± 3.89
ZI-84	31,032	81,126	4887	4	g	10.5928	0.40202	1940 ± 33	4.922 ± 0.084	50.26 ± 4.36	54.84 ± 5.51

The ages are calculated with the CRONUS 2.2 (with constants 2.2.1) calculator using the time-dependent Lal (1991)/Stone (2000) production rate model.
Shielding factor is 0.99; sample density is 2.7 g/cm^3 for granite and 2.65 g/cm^3 for quartzite.
Standard used is LLNL3000 (^{10}Be isotope ratio = 3×10^{-12}).

[a] External uncertainties (analytical and production rate) are reported at the 1 s confidence level.

[b] We applied an erosion rate of 3×10^{-4} cm/yr and subtracted mean inheritance from T0′ ($0.313\pm0.0199\times10^6$atom/g).

out, even in the absence of qualitative field evidence for such processes, particularly for old (>20 ka) surfaces. We also note that studies (especially where cosmogenic dating has been used in conjunction with different dating techniques and for various time scales) within or around the Tibetan Plateau have shown that erosion of flat alluvial terraces may be negligible. For instance, Hetzel et al. (2002) have shown that surfaces in northeast Tibet dated with ^{10}Be and ^{26}Al, together with ^{21}Ne have suffered negligible erosion over a period of 170 ka. Along the Kunlun fault, consistent slip-rates determination with ^{10}Be, ^{26}Al, ^{14}C and OSL dating indicate that erosion is negligible for Holocene alluvial fans and terraces (e.g. Li et al., 2005; Van der Woerd et al., 1998, 2002). Along the central and eastern Altyn Tagh fault, combined surface and sub-surface dating with ^{10}Be and ^{26}Al, and consistent sub-surface ^{14}C have systematically shown that erosion is negligible for late Pleistocene and Holocene alluvial terraces (e.g. Gold et al., 2009, 2011; Meriaux et al., 2004, 2005; Ryerson et al., 2006; Xu et al., 2005).

In contrast, however, most of these studies show that inheritance, although usually small, is a significant source of uncertainty in assessing surface exposure ages. The problem with inheritance is to evaluate whether it is evenly or randomly distributed in the samples. For large catchments and using an amalgamated technique, the result is usually that inheritance is an average quantity distributed evenly in all the samples (Hetzel et al., 2002). For smaller catchments, this is usually not the case and inheritance can be assessed by the occurrence of outliers within nuclide concentration distributions (e.g. Meriaux et al., 2004, 2005; Van der Woerd et al., 1998; 2002; Xu et al., 2005).

Because of probable negligible erosion (see discussion above), we favor Model 1 ages as the most likely model ages. Throughout the text, we report data for Model 1 only, while data for Model 2 are presented in the tables. Slip rates calculated using both models are similar (within <7%, Table 4) and do not change our conclusion, probably due to the fact that most of our dated features are relatively young and therefore not too affected by erosion.

For the sampled moraines, we calculated the ages assuming zero erosion (Table S1) and assess the moraine ages based on a conservative approach in which we consider both the oldest age and mean age of the samples (see Chevalier et al., 2011a, for detailed discussion). Indeed, it is still not altogether clear which of these two models may be appropriate for inferring the moraine surface exposure age from boulder ages on its surface.

4. Results

4.1. Site 1: Menshi fans

4.1.1. Geomorphology

The Menshi fans (Site 1) are located at 31°17′N–80°42′E, about 10 km northwest of the village of Menshi at an average elevation of 4700 m (Fig. 2). The fans slope at ~4° (determined from topographic maps). From surface relief, color differences on satellite images, and field observations, the piedmont appears to be composed of three surfaces: an older surface (T3–T3′), 3–8 m above an intermediate

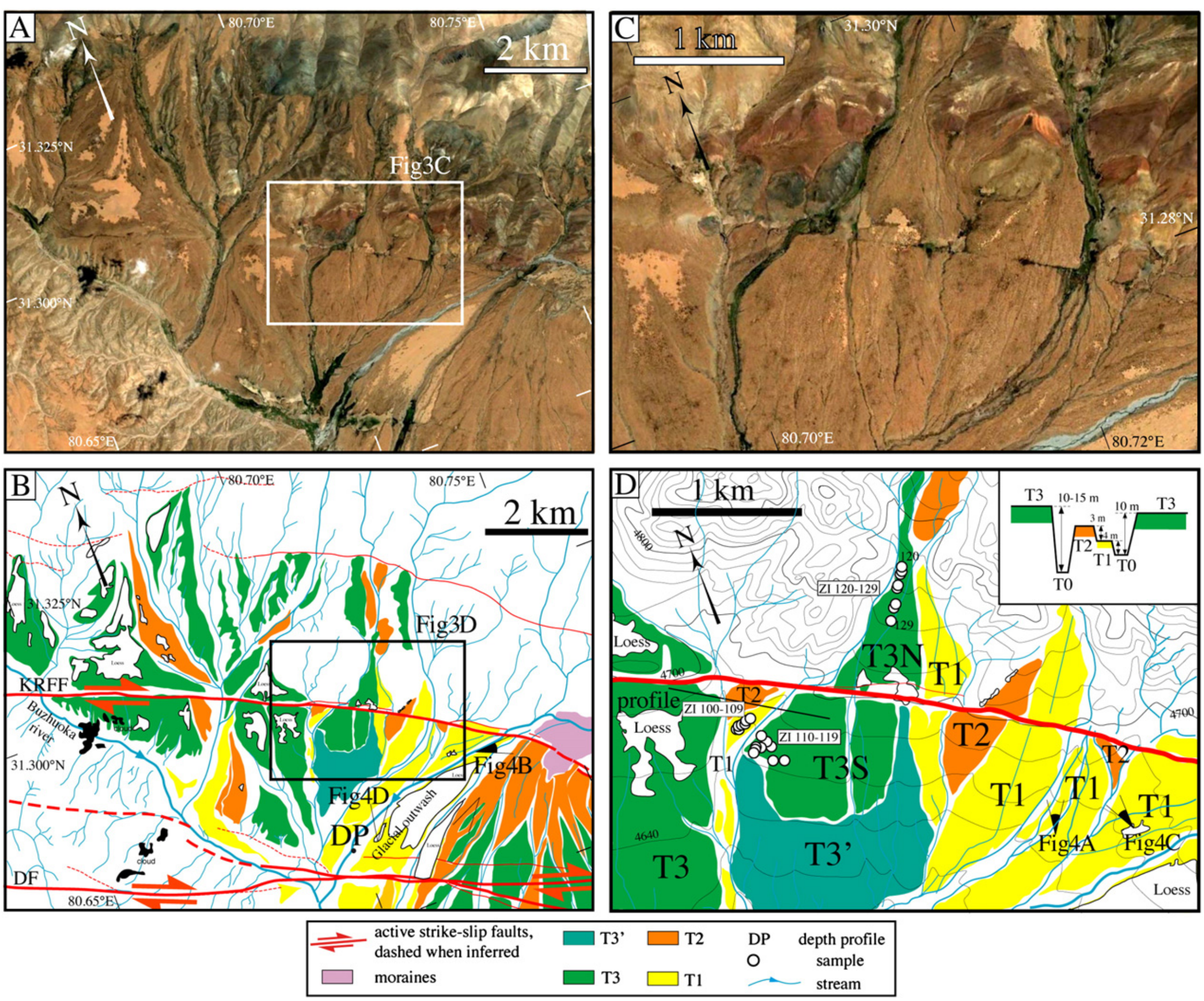

Fig. 3. Quickbird satellite image (GoogleEarth, 2009) and interpretation of Menshi (Site 1). (A,B) General active faults and geomorphological mapping of Menshi site. KRFF = Kailas Range Front fault, and DF = Darchen fault. (C,D) Close-up of the targeted surfaces along the KRFF. Inset is schematic topographic profile from west to east across the terrace/fan levels. Topographic contours every 20 m.

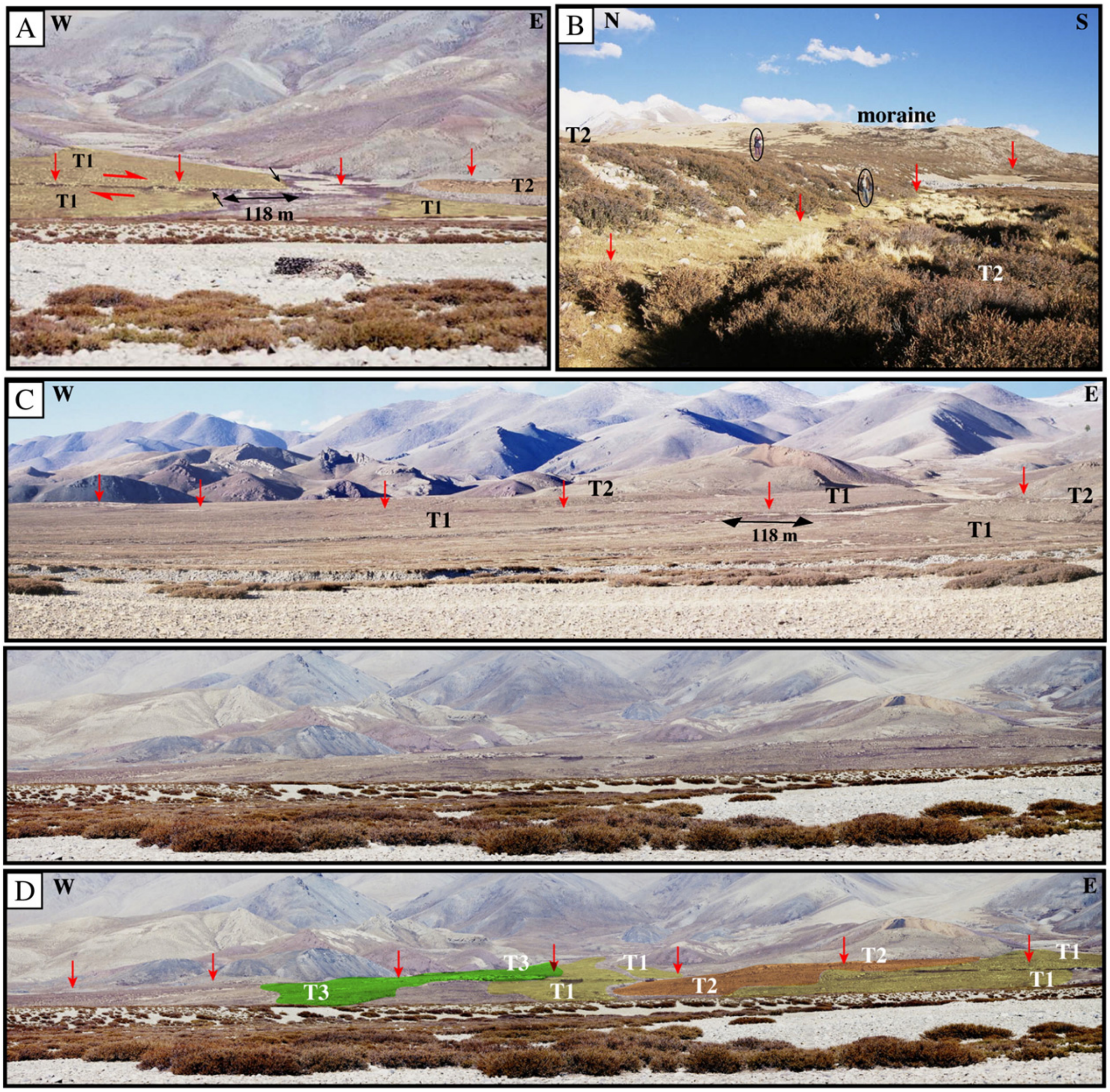

Fig. 4. Field photo of the Menshi site. (A,C) show the 118 ± 18 m offset by the KRFF of T1 fans. (B) shows the scarp (~2.5 m, people circled for scale) just west of the moraine. (D) is a general view of the site where T3, T2 and T1 are labeled. Photo locations are shown in Fig. 3B,D.

one (T2) and 6–11 m above a younger one (T1) (Fig. 3). The fan and terrace surfaces are covered by sub-angular pebbles and cobbles, indicative of a proximal origin and are partly covered by grass or small bushes. Light gray patches on the surfaces (visible on the satellite images of Fig. 3) correspond to thin sand/loess deposits. A larger, light-colored triangular patch is a glacial outwash surface, fed by a large catchment composed of 4 former glacial valleys. Lateral and frontal moraines sourced from the largest, easternmost glacier, whose remnant terminus is located at the outlet of a glacial cirque at 5550 m, appear to have previously reached the fault (Figs. 3A,B and 4B). In this area, two main strands of the Karakorum fault, the western segments of the KRFF and DF, are sub-parallel ~N110°E striking faults that cut and offset fans and terraces in the piedmont of the western part of the Kailas Range (Figs. 2 and 3).

4.1.2. Offsets

Along the KRFF, two cumulative offset values can be measured by realigning displaced fan edges, terrace risers and river channels on the satellite images and 1/50,000 topographic maps. Building on Liu (1993)'s work, who did not have access to the field, a first set of offsets is associated with T1 surfaces and a second set of offsets, somewhat less clear, is associated with T3 surfaces. The first set of similar right-lateral offsets average at about 118 ± 18 m (Figs. 3–5). Retro-deforming the images by 98 to 138 m realigns the edges of the T1 fan surfaces and some channel courses, as well as some drainages present on these surfaces (Fig. 5). The set of larger offsets of about 430 ± 30 m realigns the edges of the older surface T3 to the west, and at a larger scale, it also straightens the course of the Buzhuoka River (Fig. 6).

The DF splits into two branches west of the Buzhuoka River (Fig. 3B). To the east, the main DF is a clear single trace fault for about 2 km, then it splits again into two branches. Another more subdued fault trace can be seen on the high-resolution images about 300 m to the north, which becomes more important eastward (Fig. 3A,B). While the DF cuts through the T0 and T1 levels, no clear offset can be measured because the risers have complex geometries

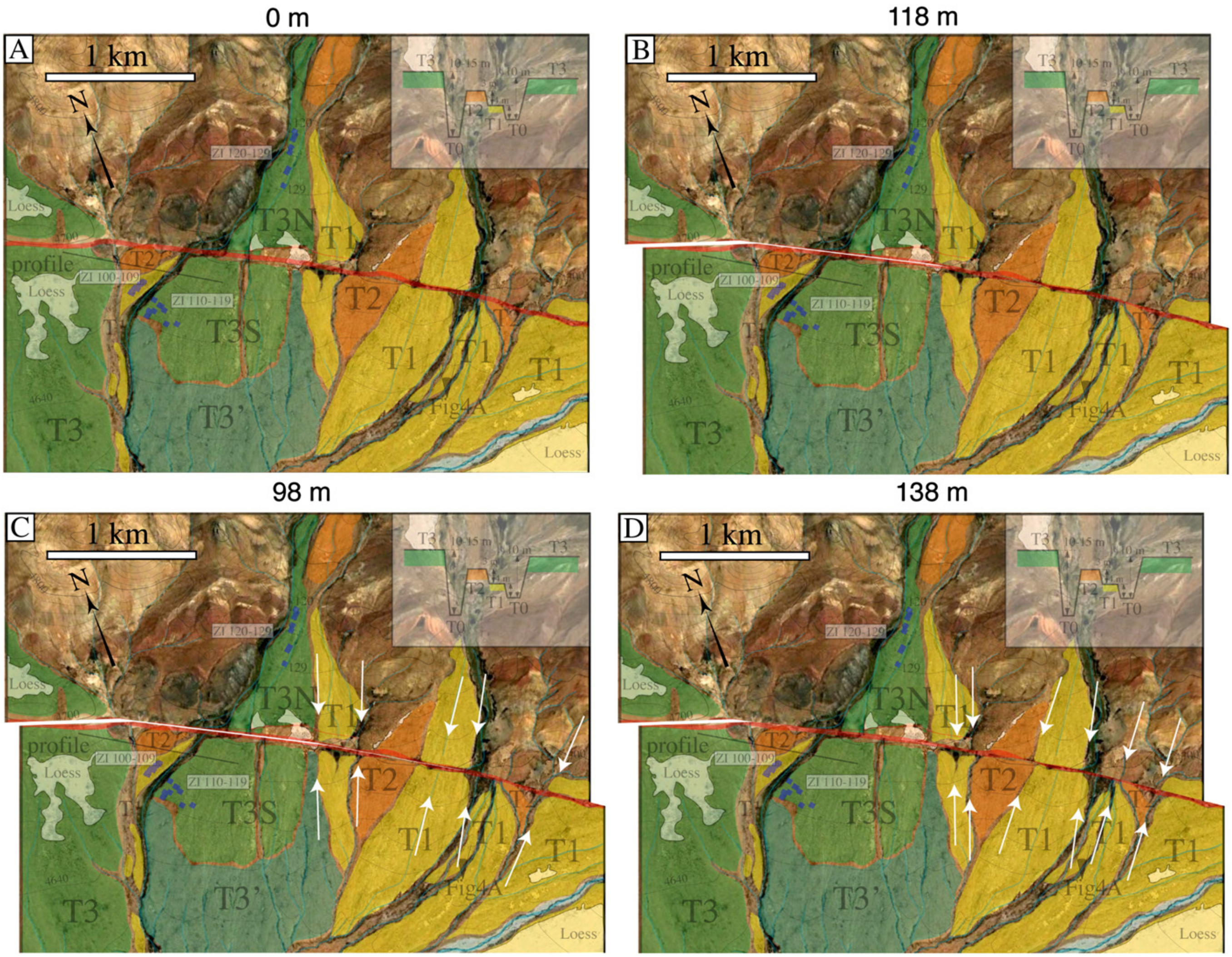

Fig. 5. Smaller offset reconstruction at Menshi site. Retro-deforming the images by 118 ± 18 m along the KRFF realigns the edges of the T1 fans and some drainages on T1 surfaces.

or are degraded by meandering drainages. Further east, the eastern edge of the glacial outwash terrace T1 is cut and right-laterally offset by the fault 188 ± 18 m (Fig. 6).

4.1.3. Surface ages

Twenty-eight samples (mostly granite cobbles) were collected on T1 and T3 (ZI-100 to ZI-129, white circles in Fig. 3D). South of the fault, 8 samples were collected on T1 (ZI-100 to ZI-109) and 10 on T3 (T3S, ZI-110 to ZI-119). Ten additional samples were collected on T3 north of the fault (T3N, ZI-120 to ZI-129).

Of the 8 samples collected on T1, 2 (ZI-107 and 108, white in Fig. 7) are about twice as old as the next oldest age of the remaining 6 samples, and can be considered outliers (Putkonen and Swanson, 2003). The 6 remaining samples yield a median age of $24.1^{+11.3}/_{-5.1}$ ka (Fig. 7, Tables 1 and 4). On T3, the range of ages stretches from 33 to 206 ka (100% of the samples) or 49 to 151 ka (90%) when the 2 extreme samples are excluded (ZI-111 and 118, white in Fig. 7), yielding a median age of $107.6^{+29.7}/_{-37.6}$ ka. If taken separately, all samples on T3N average at $98.5^{+29.0}/_{-30.7}$ ka while all samples but the 2 youngest and the oldest one on T3S (ZI-111, 112 and 118) average at $123.1^{+27.1}/_{-22.0}$ ka (Fig. 7, Tables 1 and 4).

The ages of T1 and T3 may be compared to those of climatic periods defined in relation with global climate change. For this purpose, we plotted both the SPECMAP δ^{18}O proxy curve and the Marine Isotope Stages, as alternating white and gray-shaded sectors (MIS, Imbrie et al., 1984) in Fig. 7. The average age of T3 would correlate with deposition during the MIS-5 interglacial (Eemian stage). On T1, a few sample ages postdate the Last Glacial Maximum (LGM, ~20 ka) and a few others postdate the MIS-3 glacial (~40 ka), suggesting again that the emplacement of these samples took place during warm and humid interstadials or interglacials, periods generally considered favorable to fluvial deposition.

Results from the depth profile (within the glacial outwash) are discussed in the supplemental material, due to data scatter and the too-small number of clasts sampled, which do not allow an accurate constraint of the surface age.

4.2. Site 2: La Zhi Tang terraces

4.2.1. Geomorphology

The La Zhi Tang site (Figs. 2 and 8) is located at 31°2′N–81°8′E, at an elevation of 4900 m, 15 km west of Mount Kailas. Here, an alluvial fan and inset terraces were emplaced by the Tu Qiong glacial outwash river, downstream from where it breaches the terminal moraine complex abandoned at the extremity of the ~25 km-long, U-shaped, Tu Qiong glacial valley (Fig. 2), at the outlet of which lies the Kailas Range Front fault (KRFF).

In contrast to the large south-facing faceted spurs along the KRFF (Fig. 2), a north-facing, 1–2 m-high scarp marks the trace of the

Table 3
Analytical results of ^{10}Be geochronology of the Rengongpu terraces in the Pulan graben and surface exposure ages.

Sample name	Lat (N)	Long (E)	Elev (m)	Thickness (cm)	Quartz/ granite	Quartz (g)	Be carrier (mg)	$^{10}Be/^{9}Be$ 10^{-15}	^{10}Be (10^6 atom/g)	Model 1 LS dep Ages (ka)[a]	Model 2 LS dep Ages (ka)[a,b]
T3											
KC2-7	30,435	81,159	4410	8	g	10.14	0.443	865 ± 14	2.525 ± 0.043	35.66 ± 3.09	37.39 ± 3.63
KC2-8	30,435	81,159	4410	6	g	10.08	0.454	618 ± 14	1.861 ± 0.043	26.84 ± 2.36	27.29 ± 2.65
KC2-9	30,435	81,159	4410	3	g	10.01	0.439	1061 ± 37	3.11 ± 0.11	40.74 ± 3.76	43.79 ± 4.59
KC2-10	30,435	81,159	4410	5	g	5.10	0.442	322 ± 7	1.869 ± 0.045	26.75 ± 2.36	27.19 ± 2.65
KC2-11	30,435	81,159	4410	7	g	10.06	0.436	704 ± 19	2.042 ± 0.056	29.34 ± 2.62	30.15 ± 2.98
KC2-12	30,434	81,159	4410	10	g	7.51	0.444	778 ± 18	3.07 ± 0.072	42.29 ± 3.74	45.88 ± 4.62
KC2-13	30,434	81,159	4410	5	g	11.08	0.436	916 ± 19	2.411 ± 0.051	33.55 ± 2.94	35.08 ± 3.42
KC2-14	30,434	81,159	4410	5	q	11.37	0.445	743 ± 25	1.942 ± 0.067	27.65 ± 2.53	28.18 ± 2.86
KC2-15	30,434	81,159	4410	7	g	11.13	0.437	1047 ± 20	2.748 ± 0.053	37.88 ± 3.3	40.09 ± 3.93
KC2-16	30,435	81,159	4410	6	g	11.06	0.444	1161 ± 21	3.115 ± 0.056	41.64 ± 3.62	45.01 ± 4.45
T2											
KC2-17	30,433	81,159	4380	4	q	6.00	0.427	147 ± 5	0.7 ± 0.023	10.69 ± 0.97	9.49 ± 1.07
KC2-18	30,433	81,160	4380	3	g	2.71	0.448	30 ± 3	0.332 ± 0.034	5.18 ± 0.69	3.86 ± 0.87
KC2-19	30,433	81,160	4380	5	q	11.00	0.452	287 ± 7	0.79 ± 0.021	12.17 ± 1.08	11.01 ± 1.17
KC2-20	30,433	81,160	4380	5	g	11.24	0.436	153 ± 4	0.398 ± 0.01	6.17 ± 0.54	4.91 ± 0.74
KC2-21	30,433	81,160	4380	5	g	5.52	0.462	77 ± 3	0.43 ± 0.021	6.63 ± 0.65	5.39 ± 0.81
KC2-22	30,433	81,160	4380	6	g	8.42	0.445	149 ± 4	0.529 ± 0.014	8.16 ± 0.72	6.85 ± 0.85
KC2-23	30,433	81,159	4380	6	g	8.92	0.445	200 ± 4	0.667 ± 0.016	10.36 ± 0.91	9.1 ± 1.01
KC2-24	30,433	81,159	4380	5	q	10.05	0.427	189 ± 5	0.537 ± 0.014	8.22 ± 0.72	6.92 ± 0.85
KC2-24bis*	30,433	81,159	4380	5	q	10.09	0.462	180 ± 5	0.55 ± 0.017	8.41 ± 0.75	7.11 ± 0.87
KC2-25	30,433	81,159	4380	5	g	7.34	0.437	155 ± 4	0.617 ± 0.018	9.51 ± 0.85	8.17 ± 0.95
KC2-26	30,433	81,160	4380	4	q	8.37	0.450	103 ± 4	0.371 ± 0.017	5.76 ± 0.55	4.47 ± 0.74
T1											
KC2-28	30,432	81,157	4330	7	g	7.70	0.451	89 ± 2	0.348 ± 0.011	5.69 ± 0.51	4.33 ± 0.74
KC2-33	30,432	81,157	4330	5	g	10.07	0.458	114 ± 3	0.346 ± 0.01	5.57 ± 0.49	4.22 ± 0.72
KC2-35	30,432	81,157	4330	7	g	10.12	0.445	123 ± 4	0.361 ± 0.011	5.87 ± 0.53	4.53 ± 0.75
T0											
KC2-37	30,429	81,157	4320	5	q	10.14	0.435	7 ± 1	0.022 ± 0.005		
KC2-38A	30,429	81,157	4320	7	g	11.35	0.438	42 ± 2	0.108 ± 0.007		
KC2-38B	30,429	81,157	4320	5	g	9.97	0.444	70 ± 2	0.209 ± 0.008		
KC2-38C	30,429	81,157	4320	6	g	4.57	0.436	162 ± 7	1.05 ± 0.047		
KC2-38D	30,429	81,157	4320	5	g	4.53	0.440	5 ± 5	0.034 ± 0.033		

Some samples on T0 may have been pre-exposed before being incorporated in the terrace deposits. The large scatter in these concentrations, together with the presence of very low concentrated samples, makes it difficult to calculate an average inheritance.
The ages are calculated with the CRONUS 2.2 (with constants 2.2.1) calculator using the time-dependent Lal (1991)/Stone (2000) production rate model.
Shielding factor is 0.99; sample density is 2.7 g/cm^3 for granite and 2.65 g/cm^3 for quartzite. Standard used is KNSTD (^{10}Be isotope ratio = 3.11×10^{-12}). * Sample KC2-24 on T2 was processed twice (KC2-24bis), which yielded a conclusive test of the age measurement reproducibility.
[a] External uncertainties (analytical and production rate) are reported at the 1 s confidence level.
[b] We applied an erosion rate of 3×10^{-4} cm/yr and subtracted mean inheritance from T0 ($0.093 \pm 0.035 \times 10^6$ atom/g), excluding outlier KC2-38C.

Darchen fault (DF) across the terrace surfaces west of the outwash (Figs. 8 and 9), attesting to a small component of uplift south of the fault. Clear right-lateral offsets of risers and channels are observed on each side of the outwash (Figs. 8–10). Two main sets of terraces (T1 and T2) are visible. A ~80 m-wide, ~250 m-long pull-apart basin has formed within the highest terrace (T2) ~500 m west of the river (Figs. 8 and 9A,C). The active outwash river-bed (T0) is vertically entrenched ~15 m into the T1 terrace complex (inset in Fig. 8B and photos in Fig. 9A,F), upon which a bar and swale morphology, as well as small risers, are still preserved. The T2/T1 riser is about 4 m high. Several inset terrace risers are visible on the eastern bank of the river, but the intervening terraces, which directly abut moraine deposits, form very narrow benches (Fig. 8A,B). All the terrace surfaces are covered by 10–25 cm diameter granite cobbles (Fig. 9).

4.2.2. Offsets

We measured cumulative dextral offsets west of the outwash by realigning risers or channels in the field and on the 1 m-resolution Quickbird images. We determined T2/T1s fan edge (i.e. naturally curved) offset by projecting the correlative edge crests (not the base due to degradation over time) to the DF trace and measuring the range of horizontal offsets. We considered a near-the-fault projection and a projection from further away for both risers (Gold et al., 2011). By doing so, minimum and maximum offsets were determined (Fig. 8D). The reported offset (80 ± 20 m) is the mean value between the minimum (60 m) and maximum (100 m) measured offsets, with an uncertainty that is one-half of this range. Due to the presence of the pull-apart and the vertical component of slip on the strike-slip fault, a small fan has developed north of T1″, probably covering the initial morphology of terrace risers. Indeed, no corresponding T1″ level is recognized north of the fault, attesting that T2/T1s offset is a minimum. However, T1′ and T1 are both visible north and south of the fault.

A channel incised at the eastern limit of the small fan north of the fault is offset by about 24 ± 2 m, and then follows the base of the T1″/T1′ riser south of the fault and may be taken as a maximum offset for T1″ (Fig. 8). The T1′/T1 riser is well developed on both sides of the fault and is offset by 18 ± 2 m (Figs. 8 and 9A–C,E). A channel incised within T1 is offset by 10 ± 1 m and the T1/T0′ riser is offset by about 7 ± 1 m (Figs. 8 and 9A,C,D). These well-defined, smaller, riser offsets have been measured in the field with a tape.

West of T2, two small, south-flowing, surface rill channels, which are both offset by ~80 m as they cross the fault, are realigned by the same amount of back-slip that restores the T2/T1s riser (Fig. 10B). A larger offset (220 ± 20 m) is required to realign one prominent stream channel farther west (Fig. 10C). Up-valley from the La Zhi Tang site, we find a ~270 ± 30 m offset (measured from the satellite images) along the KRFF of the west Tu Qiong lateral moraine. Unfortunately, we did not collect any samples from that moraine surface.

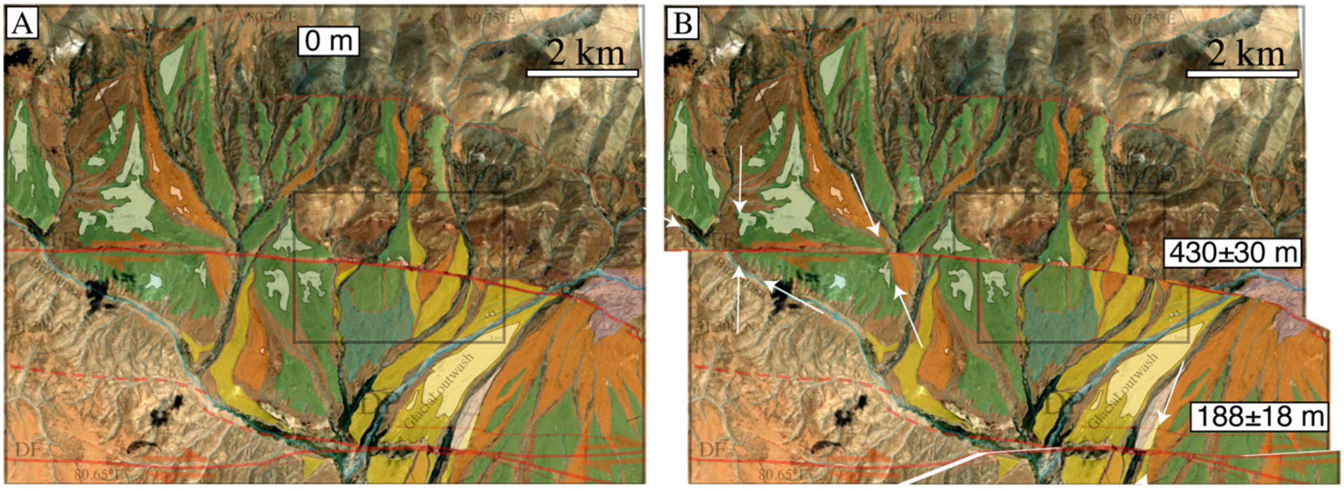

Fig. 6. Larger offset reconstruction at Menshi site. (A) Menshi site today. (B) 430 ± 30 m of image retro-deformation along the KRFF realigns the Buzhuoka River to the west and the edges of the older T3 surface. A 188 ± 18 m retro-deformation along the DF realigns the eastern riser of the glacial outwash.

4.2.3. Surface ages

A total of 31 cobbles were collected on the La Zhi Tang terraces (Fig. 8): 4 samples on T0', in the active river-bed (24LQ-T0.1 to 24LQ-T0.4); 8 samples on T1 (4 north of the fault, ZI-75-79 and 4 south of the fault, ZI-65-69); 8 samples on T1′ (4 north of the fault, ZI-70-74 and 4 south of the fault, ZI-60-64); 5 samples on T1″ south of the fault (ZI-55-59) and 6 samples on T2 (3 north of the fault, ZI-80-84 and 3 south of the fault ZI-50-53). T2N was sampled well north of the pull-apart to avoid collecting post-depositional or eroded samples. Sixteen ages (76%) on T1, T1′ and T1″ are tightly clustered excluding 5 outliers (white in Fig. 11). T1 average age is 10.5$^{+1.8}/_{-1.3}$ ka, T1′ is 11.1$^{+1.2}/_{-1.4}$ ka and T1″ is 12.3$^{+1.4}/_{-1.3}$ ka. The ages on T2 range from 39 to 62 ka with an average of 49.9$^{+12.6}/_{-9.0}$ ka (Fig. 11, Tables 2 and 4).

The ages of T1 and T2 may be compared to those of climatic periods defined in relation with global climate change. For this purpose, we plotted the Marine Isotope Stages (MIS), as alternating white and gray-shaded sectors (Imbrie et al., 1984) in Fig. 11. The well-defined cluster at ~10–12 ka on T1s defines an unambiguous emplacement age during the Early Holocene Climatic Optimum, a warm and humid pluvial that has now been demonstrated to be a major period of fan deposition and terrace aggradation in other parts of Tibet (e.g. Gasse et al., 1991; Meriaux et al., 2004, 2005; Van der Woerd et al., 1998, 2000). The somewhat scattered age on T2 could correlate with deposition during the Early MIS-3 interstadial (Fig. 11).

4.3. Sites 3 and 4: A Qu, West and East Xiong Se moraines

4.3.1. Geomorphology

The A Qu, West and East Xiong Se moraine sites have been previously described in detail in Section 3.1.6 in Chevalier et al. (2011a), and studied for climatic purposes. The A Qu lateral moraines are located 5 km southeast of the La Zhi Tang terraces (Figs. 2 and 12), with their lowermost frontal lobe that once encroached upon the trace of the DF. Large (500 m-high) triangular facets, attesting to a vertical throw component on the KRFF, are visible along the range-front (Fig. 12). The West Xiong Se and East Xiong Se lateral moraines are located 6 km east of the A Qu moraines (Figs. 2 and 12) and are cut by both main strands of the Karakorum fault (KRFF and DF), but additional minor strands are also visible. Field photos showing surface boulders and moraine crests are visible in Fig. 13.

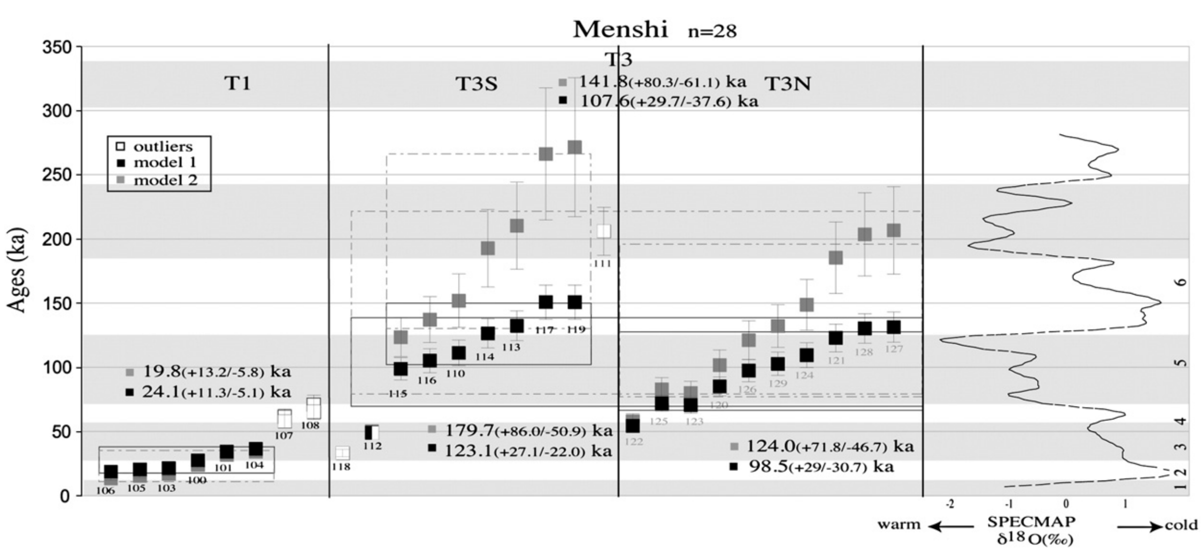

Fig. 7. Ages of the Menshi samples. Model 1 ages refer to ages calculated with no erosion and no inheritance subtracted, while Model 2 ages refer to ages calculated with erosion and inheritance (from the deepest sample in the depth profile) subtracted. Median ages (calculated using the method of Zechar and Frankel, 2009) for both models are indicated as boxes (dashed for Model 2), with 1-sigma (s) uncertainty. The gray-shaded sectors are the Marine Isotope Stages (MIS) of Imbrie et al. (1984) with the corresponding periods presented by the numbers on the right, as well as the Specmap climatic proxy curve.

4.3.2. Offsets

Back-slipping the Quickbird image and the 1/50,000 topographic map by 250 ± 50 m realigns the crest of the western A Qu lateral moraine south of the KRFF with the sharp edge of the glacial bedrock incision north of the fault (Fig. 14A,B,C). The West Xiong Se lateral moraine is also offset right-laterally from the edge of glacial incision in the Xiong Se valley by the KRFF. Retro-deformation of the Quickbird and 1/100,000 topographic maps constrains an offset of 340 ± 40 m (Fig. 14D,

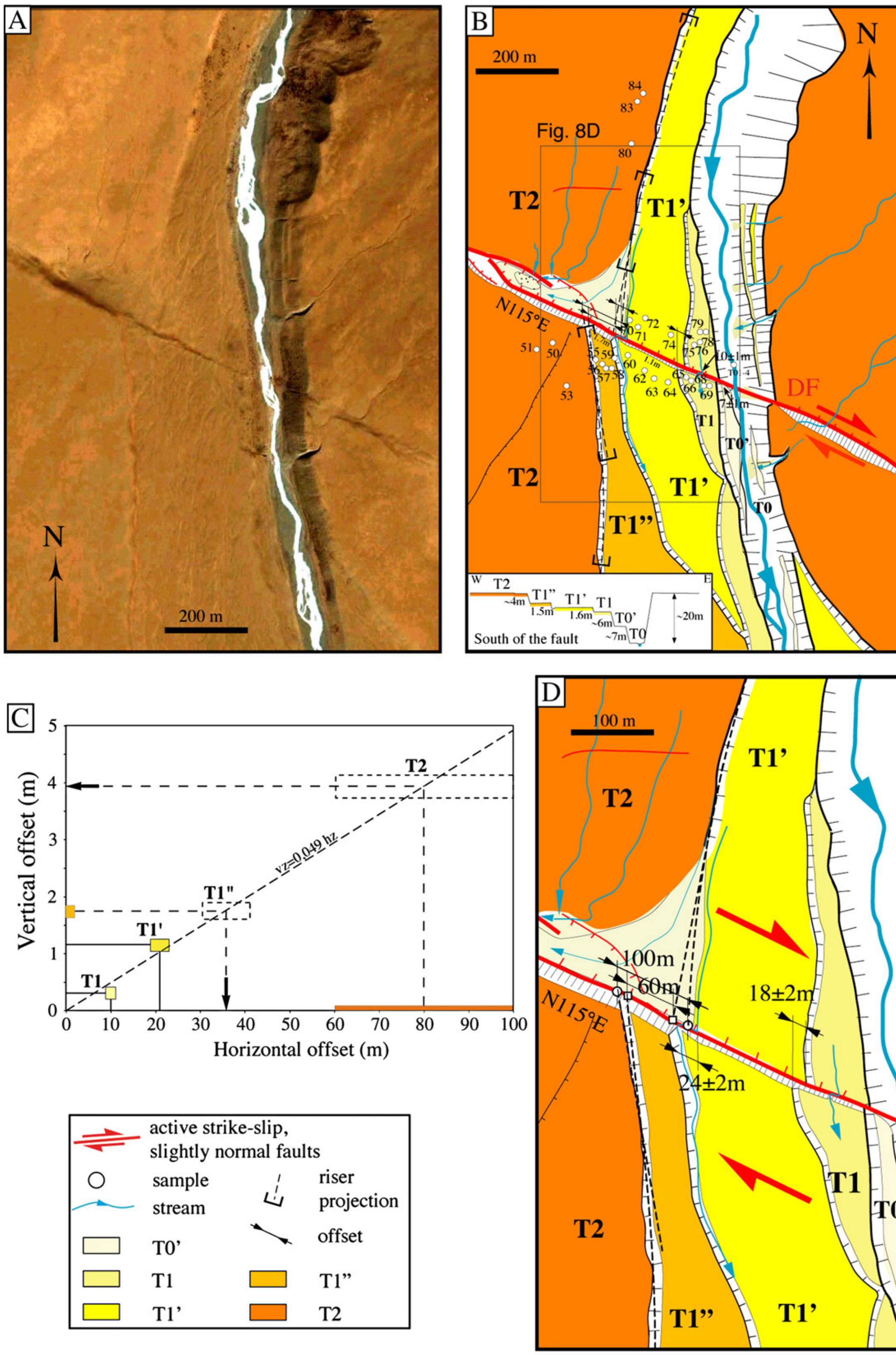

Fig. 8. Quickbird satellite image and interpretation of La Zhi Tang (site 2). (A,B) Geomorphological mapping of site 2. Inset is a schematic section from west to east across the terrace levels. All terraces are cut and offset by the Darchen fault (DF). The T1–T1′–T1″ levels are offset between 7 and 24 m, while the higher T2/T1″ edge is offset about 80 m (see the different edge projections on the close-up on D). (C) Vertical vs. horizontal offsets at La Zhi Tang. (D) Close-up of the largest offset and its projections from different distances from the fault.

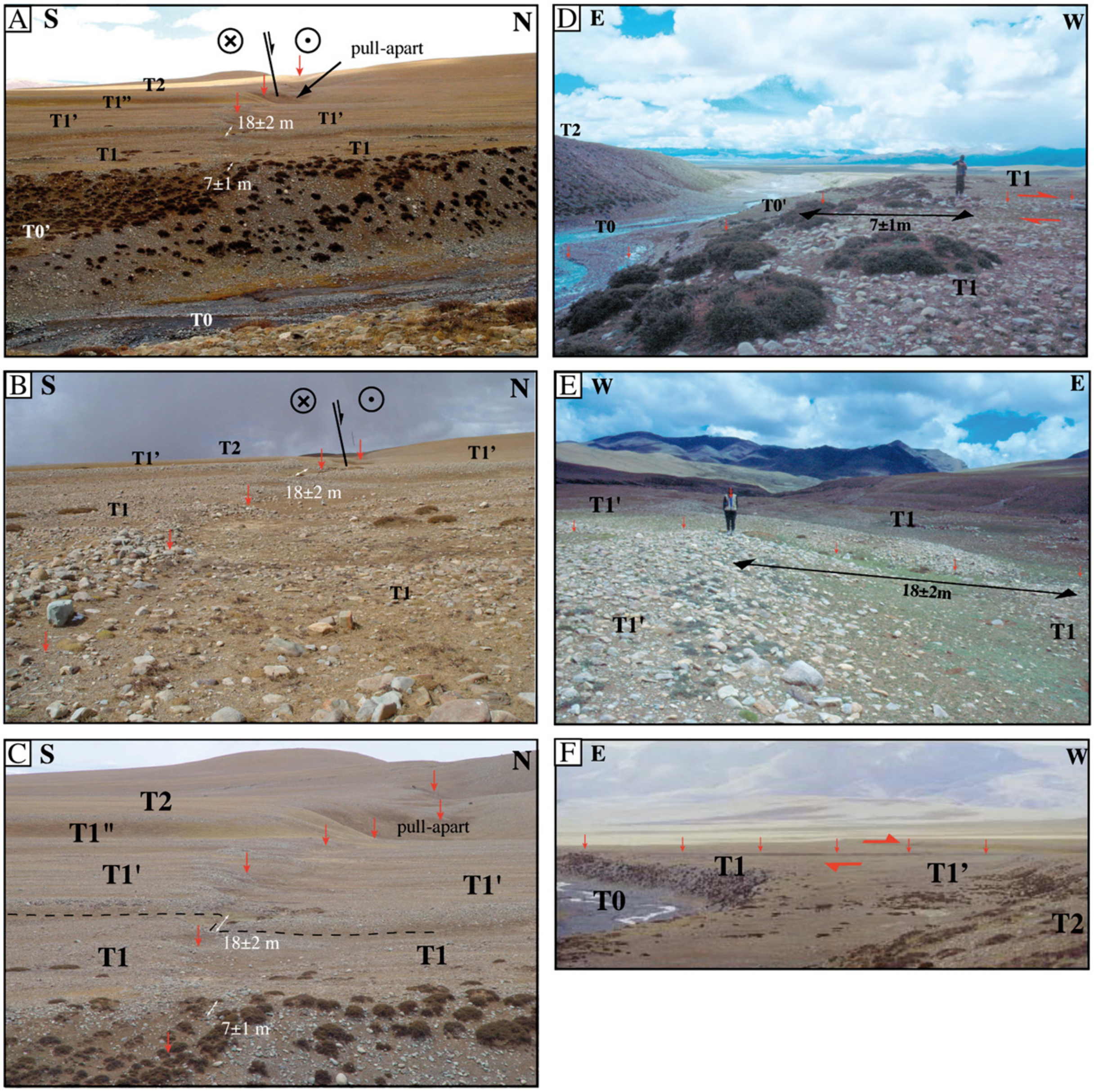

Fig. 9. Field photos at La Zhi Tang. Fault trace is highlighted by red arrows, with southern side up (A,B,C,F). (A–E) show the 7 ± 1 m offset of T1/T0′ riser and 18 ± 2 m offset of T1′/T1 riser. Pull-apart is visible on (A,C).

E,F). A smaller offset (90 ± 40 m) by the same fault, of the East Xiong Se moraine can also be measured (Fig. 14G), however it is harder to constrain.

4.3.3. Surface ages

Seven embedded boulders were collected on the crest of the western A Qu lateral moraine (KC2-75-83 from south to north). Fourteen and 8 boulders were collected from south to north, on the crests of the West and East Xiong Se lateral moraines, respectively (ZI-85-99 and KC2-66-74, Figs. 12 and 15, Table S1 for ages calculated using the 4 production rate scaling models; and Table S1 in Chevalier et al., 2011a, for sample details).

The emplacement age of the East Xiong Se lateral moraine (EXS) may be taken as the average age of the 8 samples collected, 15.4 ± 2.1 ka, while the oldest age is 17 ± 2 ka. On the western A Qu lateral moraine, one sample age (203 ± 18 ka), which is much more than twice the age of the oldest age of the distribution (Putkonen and Swanson, 2003), is considered an outlier and ignored (white in Fig. 15). The next oldest boulder age (37 ± 3 ka) is thus taken to represent the emplacement age of this moraine, on which the average age of the other 6 samples collected is $27.6^{+7.5}/_{-5.7}$ ka. For the West Xiong Se lateral moraine (WXS), one can similarly take the age of the oldest sample (48 ± 4 ka) as the emplacement age, while the average age of the 14 samples collected is $37.2^{+7.1}/_{-14.6}$ ka.

The oldest age taken for the A Qu moraine (37 ± 3 ka) would be consistent with an emplacement during the penultimate coldest period of the last glacial cycle (late MIS-3, ~40 ka), as documented by global climate proxy curves (Imbrie et al., 1984). The bimodal distribution (two peaks at ~23 ka and ~34 ka) might reflect that it was not completely abandoned until the onset of post-LGM warming after ~20 ka (Chevalier et al., 2005a). Similarly, the oldest age of the East Xiong Se moraine (17 ± 2 ka) fits quite well with an emplacement during the LGM (MIS-2, ~20 ka). Most likely, the Xiong Se glacier withdrew rapidly at the end of the LGM, abandoning most boulders on its inner, eastern moraine before 17 ka. A correlation with the climatic proxy curve for the West Xiong Se moraine is not as straightforward. Even though one might consider its emplacement

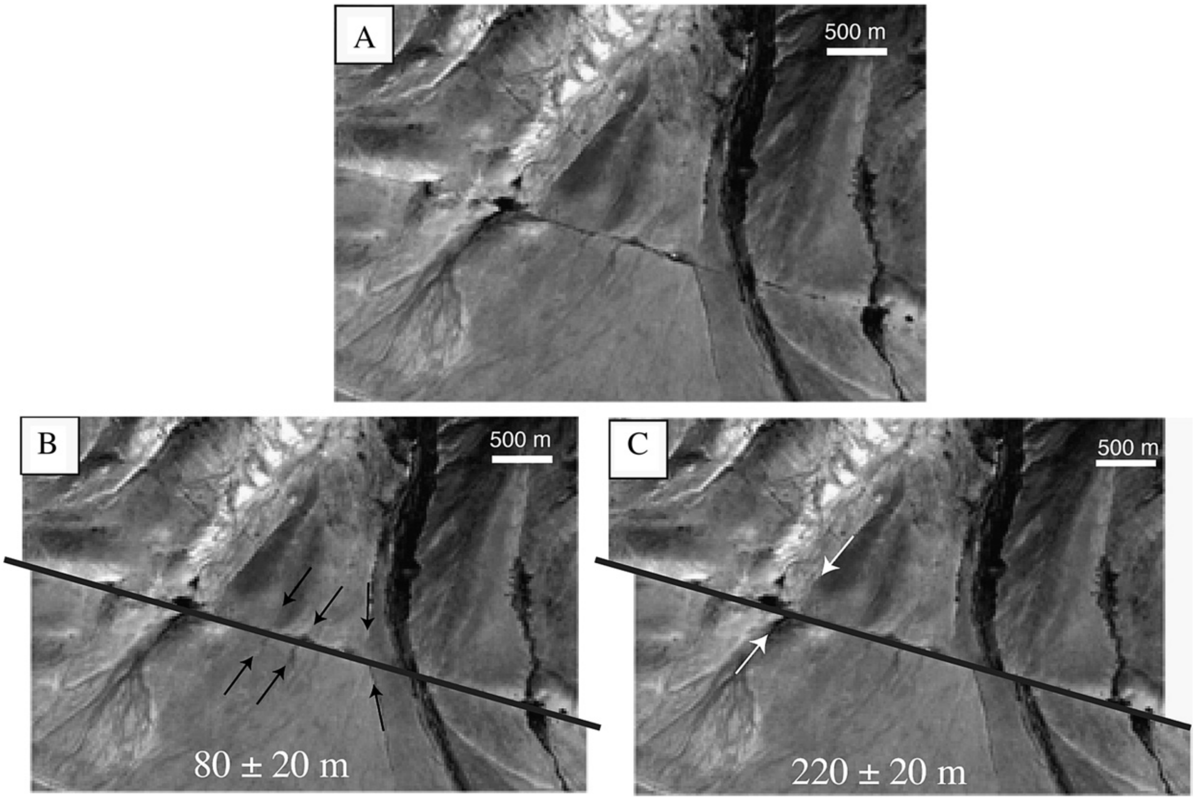

Fig. 10. Offset reconstruction at La Zhi Tang. (A) Present-day SPOT image (#212–287, 1989). (B) 80 ± 20 m offset by the DF of the T2/T1″ riser as well as two other small river channels to the west (black arrows). (C) 220 ± 20 m offset by the DF of one prominent stream channel farther west.

age to be similar to the A Qu emplacement age (~40 ka, MIS-3), we also observe a bimodal distribution at ~20 ka (LGM) and ~40 ka (MIS-3), similar to what Chevalier et al. (2005a) found at Manikala, further north, suggesting that it might not have been completely abandoned until the onset of post-LGM warming after ~20 ka.

However, Heyman et al. (2011) recently explained that the most important factor disturbing an age distribution on a moraine surface is an incomplete exposure due to post-depositional shielding (yielding exposure ages that are too young) rather than exposure prior to glaciation (yielding exposure ages that are too old). The oldest exposure age should therefore, in the absence of independent indications of prior exposure, be viewed as a minimum deglaciation age (e.g. Heyman et al., 2011 and references therein).

4.4. Site 5: Pulan graben: Rengongpu terraces

4.4.1. Geomorphology

The Rengongpu terraces are a series of fluvial terraces located at 30°26′N–81°9′E, at an elevation of ~4350 m, about 15 km north of the town of Pulan, near the border with Nepal (Fig. 2). They have been emplaced on the floor and shoulders of the active, ~NS-trending Pulan half-graben that follows the western edge of the Gurla

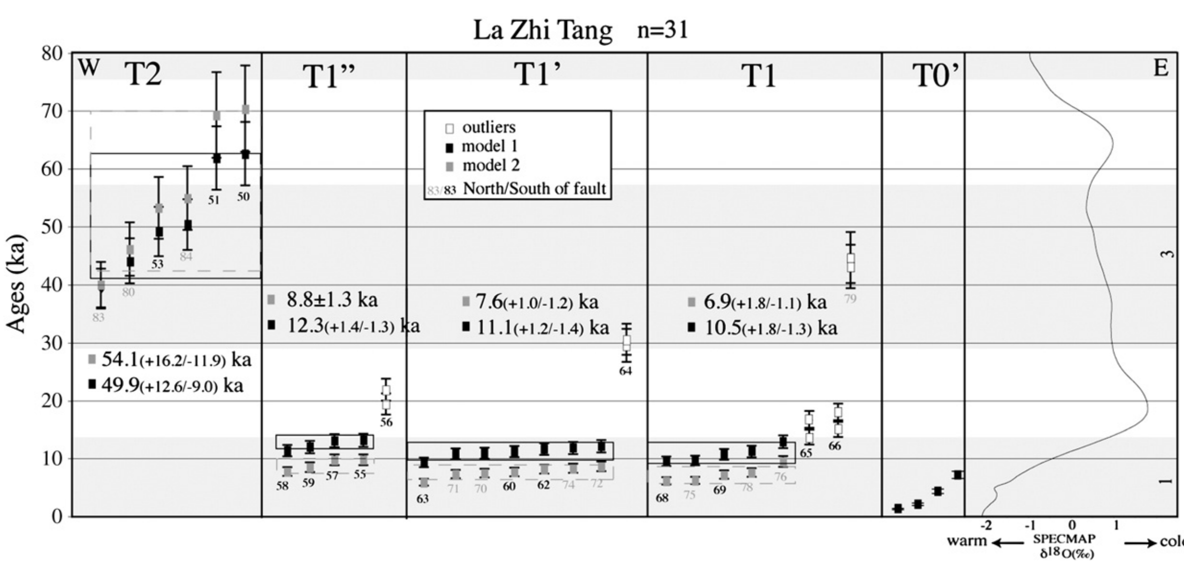

Fig. 11. Ages of the La Zhi Tang samples. Same as in caption to Fig. 7 but with Model 2 ages referring to ages calculated with erosion and inheritance from T0′ subtracted.

Table 4
Slip-rates at the Menshi site, La Zhi Tang fans, A Qu, West Xiong Se and East Xiong Se moraines along the Karakorum fault, and at Rengongpu in the Pulan half-graben.

	Offset (m)	Model 1 age (ka)						Model 1 slip-rate (mm/yr)				
		Mean	Mode	Median	68.27% interval	95.45% interval		Mean	Mode	Median	68.27% interval	95.45% interval
Menshi KRFF												
T1	118 ± 18	26.3	19.86	24.1	+ 11.3/−5.1	+ 16.1/−7.5		4.8	3.5	**4.7**	+ 1.8/−1.4	+ 3.5/−2.2
(T3)	(430 ± 30)	(105.4)	(104.92)	(107.6)	(+ 29.7/−37.6)	(+ 54.5/−60.4)		(4.5)	(3.4)	(4.0)	(+ 2.2/−0.9)	(+ 5.3/−1.4)
(T3N)		(97.5)	(72.3)	(98.5)	(+ 29.0/−30.7)	(+ 46.9/−47.8)						
(T3S)		(124.9)	(105.63)	(123.1)	(+ 27.1/−22.0)	(+ 46.3/−4.8)						
Menshi DF												
Glacial outwash	188 ± 18	19.0–137.3 (boxcar)						3.1	1.6	**2.4**	+ 2.6/−0.8	+ 6.3/−1.1
Total slip at Menshi (2 strands)										***7.1***	***± 3.2/−1.7***	***+ 4.3/−2.5***
LZT DF												
LZT T1/T0′	7 ± 1	10.7	9.91	10.5	+ 1.8/−1.3	+ 3.6/−2.3		0.7	0.6	**> 0.7**	± 0.1	+ 0.3/−0.2
LZT T1/T0′	10 ± 1	10.7	9.91	10.5	+ 1.8/−1.3	+ 3.6/−2.3		1.0	0.9	**0.9**	± 0.2	+ 0.4/−0.3
T1′		11	11.2	11.1	+ 1.2/−1.4	+ 2.4/−2.7						
T1″		12.3	12.17	12.3	+ 1.4/−1.3	+ 2.7/−2.5						
T2		51.1	47.52	49.9	+ 12.6/−9.0	+ 20.4/−14.6						
LZT T1/T1′	18 ± 2	9.2–12.3 (boxcar)						1.7	1.6	**1.7**	+ 0.3/−0.2	+ 0.5/−0.4
LZT T1′–T1′/T1″	24 ± 2	9.7–13.7 (boxcar)						2.1	2.0	<**2.1**	± 0.3	+ 0.6/−0.5
LZT T2/T1″	80 ± 20	11.0–62.5 (boxcar)						2.7	1.6	**2.2**	+ 2.0/−0.8	+ 5.0/−1.3
LZT average										**1.5**	**+ 2.1/−0.9**	**+ 5.1/−1.5**
Kailas KRFF												
(Tu Qiong)	(270 ± 30)				(Oldest age = 40 ?)			(6.75 ?)				
A Qu	250 ± 50	28.4	22.7	27.6	+ 7.5/−5.7	+ 12.9/−8.4	Mean age	9.2	7.9	**8.9**	+ 3.2/−2.4	+ 6.4/−4.2
WXS	340 ± 40	35.5	37.68	37.2	+ 7.1/−14.6	+ 14.3/−20.8	Mean age	10.5	8.5	**9.2**	+ 5.5/−1.8	+ 12.3/−3.3
EXS	90 ± 40	15.4	15.32	15.4	± 2.1	+ 3.9/−3.7	Mean age	5.9	5.6	**5.8**	+ 2.8/−2.6	+ 6.0/−5.2
Moraines average (mean)										**8.0**	**+ 7.0/−4.0**	**+ 15.1/−7.5**
A Qu						oldest age = 37 ± 3		6.8	6.7	**6.8**	+ 1.5/−1.4	+ 3.2/−2.8
West Xiong Se						oldest age = 48 ± 4		7.1	6.9	**7.0**	+ 1.1/−1.0	+ 2.3/−1.9
East Xiong Se						oldest age = 17 ± 2		5.3	5.2	**5.3**	+ 2.5/−2.4	+ 5.1/−4.7
Moraines average (oldest)										**6.4**	**+ 2.4/−2.3**	**+ 4.6/−5.8**
Total slip at Kailas (2 strands) if mean										***9.5***	***+ 7.3/−4.1***	***+ 15.9/−7.6***
Total slip at Kailas (2 strands) if oldest										***7.9***	***+ 3.2/−2.5***	***+ 6.9/−6.0***
Pulan graben–Rengongpu												
T2E/T2W	15.3 ± 1.1	8.3	6.01	8.2	+ 2.6/−2.4	+ 4.7/−3.6		2.0	1.6	1.9	+ 0.8/−0.5	+ 1.5/−0.7
T3/T2W	53.0 ± 5.0	34.2	27.62	34	+ 7.7/−7.1	+ 13.0/−10.5		1.6	1.3	> 1.6	+ 0.4/−0.3	+ 0.8/−0.5
	Offset	Model 2 age (ka)						Model 2 slip-rate (mm/yr)				
	(m)	Mean	Mode	Median	68.27% interval	95.45% interval		Mean	Mode	Median	68.27% interval	95.45% interval
Menshi KRFF												
T1	118 ± 18	22.5	15.01	19.8	+ 13.2/−5.8	+ 18.3/−8.0		6.0	3.6	**5.7**	+ 3.0/−2.2	+ 5.5/−3.1
(T3)	(430 ± 30)	(151.3)	(131.49)	(141.8)	(+ 80.3/−61.1)	(+ 170.9/−93.2)		(3.6)	(2.0)	(3.0)	(+ 2.4/−1.1)	(+ 6.0/−1.7)
(T3N)		(132.1)	(84.28)	(124.0)	(+ 71.8/−46.7)	(+ 122.6/−70.4)						
(T3S)		(193.2)	(134.23)	(179.7)	(+ 86.0/−50.9)	(+ 163.7/−74.7)						
Menshi DF												
Glacial outwash	188 ± 18	14.0–222.1 (boxcar)						2.5	1.0	**1.6**	+ 2.4/−0.6	+ 8.5/−0.8
Total slip at Menshi (2 strands)										***7.3***	***+ 3.8/−2.3***	***+ 10.1/−3.2***
LZT DF												
LZT T1/T0′	7 ± 1	7.2	6.33	6.9	+ 1.8/−1.1	+ 3.5/−1.9		1.0	1.0	**1.0**	+ 0.3/−0.2	+ 0.5/−0.4
LZT T1/T0′	10 ± 1	7.2	6.33	6.9	+ 1.8/−1.1	+ 3.5/−1.9		1.4	1.4	**1.4**	± 0.3	+ 0.7/−0.5
T1′		7.5	7.73	7.6	+ 1.0/−1.2	+ 2.0/−2.4						
T1″		8.9	8.66	8.8	± 1.3	+ 2.4/−2.3						
T2		55.6	51.87	54.1	+ 16.2/−11.9	+ 26.8/−18.6						
LZT T1/T1′	18 ± 2	5.8–8.6 (boxcar)						2.5	2.4	**2.5**	+ 0.5/−0.4	+ 0.9/−0.7
LZT T1′–T1′/T1″	24 ± 2	6.4–10.1 (boxcar)						3.0	2.7	**2.9**	+ 0.6/−0.4	+ 1.0/−0.7
LZT T2/T1″	80 ± 20	7.5–70.3 (boxcar)						2.9	1.4	**2.0**	+ 2.5/−0.8	+ 7.4/−1.3
LZT average										**2.0**	**+ 2.7/−1.0**	**+ 7.6/−1.6**
Kailas KRFF												
Moraines average (mean)										**8.0**	**+ 7.0/−4.0**	**+ 15.1/−7.5**
Moraines average (oldest)										**6.4**	**+ 2.4/−2.3**	**+ 4.6/−5.8**
Total slip at Kailas (2 strands) if mean										***10.0***	***+ 7.5/−4.1***	***+ 16.9/−7.7***
Total slip at Kailas (2 strands) if oldest										***8.4***	***+ 3.6/−2.5***	***+ 8.9/−6.0***
Pulan graben–Rengongpu												
T2E/T2W	15.3 ± 1.1	7.0	7.1	6.9	+ 2.7/−2.4	+ 4.9/−3.8		2.5	1.8	2.2	+ 1.2/−0.6	+ 2.7/−1.0
T3/T2W	53 ± 5	36.0	28.15	35.5	+ 9.5/−8.2	+ 16.0/−12.0		1.5	1.2	1.5	+ 0.5/−0.3	+ 0.9/−0.5

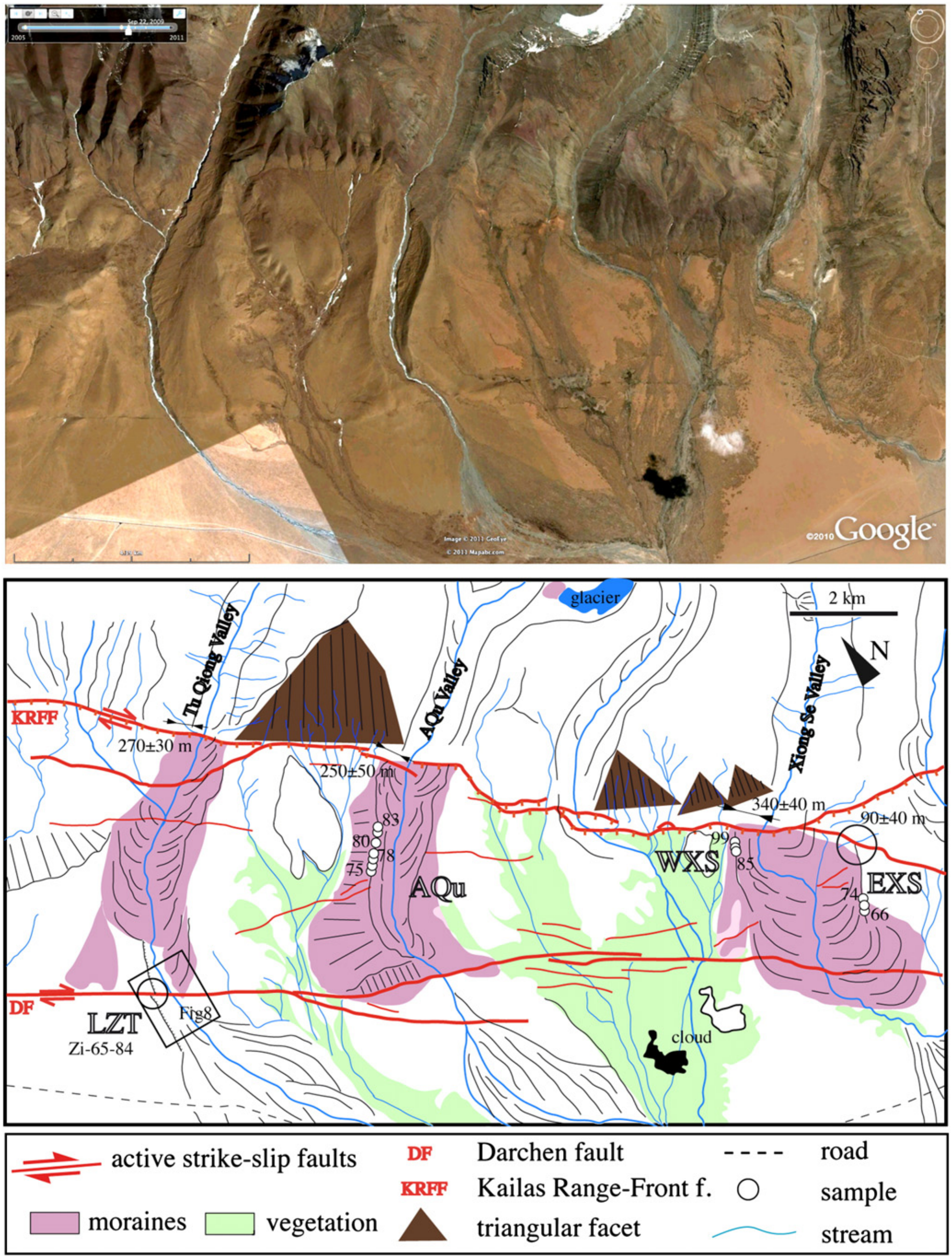

Fig. 12. Quickbird satellite image (GoogleEarth, 2005 and 2010) and interpretation of the Kailas moraines (Sites 3 and 4). WXS = West Xiong Se, EXS = East Xiong Se, LZT = La Zhi Tang.

Mandhata gneiss dome, by a glacial outwash at the outlet of a deep glacial valley originating from the edge of the 7728 m-high mountain's ice cap. The present-day glacier terminus lies 8 km upstream from the range-front, at about 5500 m.

There are 3 (possibly 4) terrace surfaces (T1 to T4), each comprising of minor sub-terraces. The principal risers are oriented EW to NE–SW (Fig. 16), roughly perpendicular to the main, ~NS-trending active faults of the Pulan half-graben. One major normal fault scarp, that of the graben's eastern master-fault (the Gurla Mandhata detachment fault), crosses and offsets the terraces. Huge (~1600 m-high) triangular facets along the western flank of the mountain attest to the important normal component of the master fault (Figs. 2 and 17A). The terrace surfaces are covered with granite/leucogranite cobbles, with no vegetation cover, except in the river-bed T0 (Figs. 16 and 17C). T3 has the steepest slope (9°), while the slopes of T2 (7°) and T1 (~5°) are shallower (Fig. 18B).

4.4.2. Offsets

Active normal faulting has raised the terrace surfaces on the footwall east of the scarp, relative to those on the hanging wall to the west (Figs. 16 and 17). Fig. 18B shows three total station profiles surveyed from a base on T1 at the top of the scarp (location in Figs. 16 and 17C), projected on a N90°E-striking section. The normal fault scarp is steep (~30–40°). Fits to the well-defined, planar terrace surfaces yield cumulative vertical throws of 15.3 ± 1.1 m and 53 ± 5 m for T2 and T3/T2, respectively. The vertical offset of T3 should be taken as a minimum, since the terrace at the base of the scarp is T2.

4.4.3. Surface ages

Twenty-nine samples on T1, T2 and T3, and in the river-bed T0 were collected (KC2-7-38 Fig. 16): 5 on T0 (KC2-37-38D) west of the fault; 3 on T1 west of the fault (KC2-28-35); 11 on T2 east of the fault (KC2-17-26) and 10 on T3 (KC2-7-16) east of the fault. The

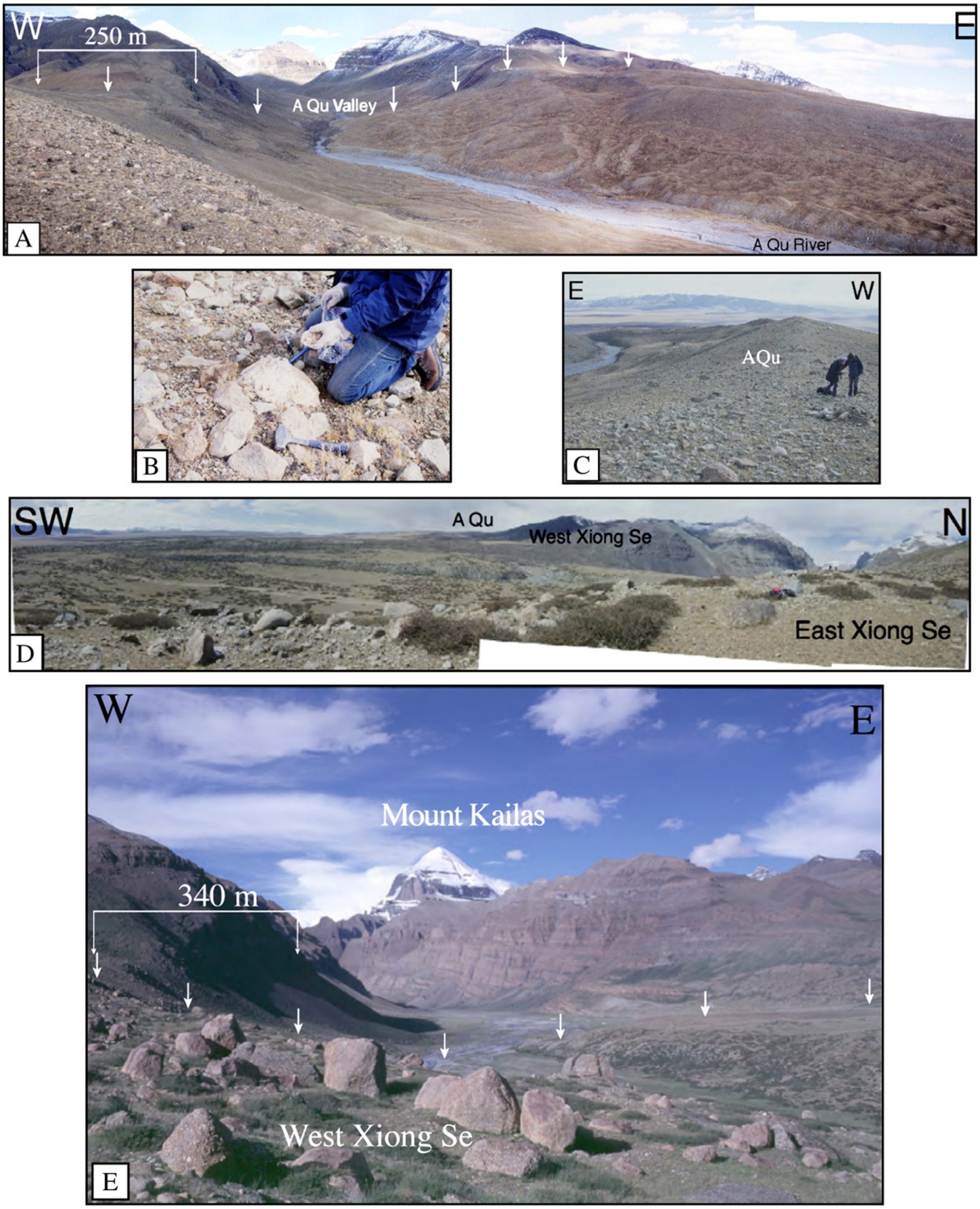

Fig. 13. Field photos of the Kailas moraines. (A–C) A Qu moraine crests and surface texture. (D) Panoramic view of the EXS and WXS moraines, with Mount Kailas to the right. The texture of the East Xiong Se moraine surface is visible. (E) View from WXS, showing large granite boulders in the foreground. White arrows show the KRFF trace.

ages on T1 and T2 cluster rather tightly at 5.7 ± 0.5 and $8.2^{+2.6}/_{-2.4}$ ka, respectively. The age scatter on T3 is larger, with values ranging from 27 to 42 ka with an average age of $34.0^{+7.7}/_{-7.1}$ ka (Fig. 19, Tables 3 and 4). The well-defined average ages of ~8 ka on T2, and ~6 ka on T1, define unambiguous emplacement ages during the early Holocene climatic optimum. For T3, the climatic correlation is not as straightforward. T3 mean age (~34 ka) postdates the MIS-3 glacial (~40 ka), suggesting that its emplacement may have taken place during the following warm and humid interstadial.

4.5. Site 6: Pulan graben: Rongguo moraines

4.5.1. Geomorphology

The Rongguo moraine site (Figs. 20 and 21) is located ~10 km north of the town of Pulan, at 30°22′N–81°10′E. It is described in

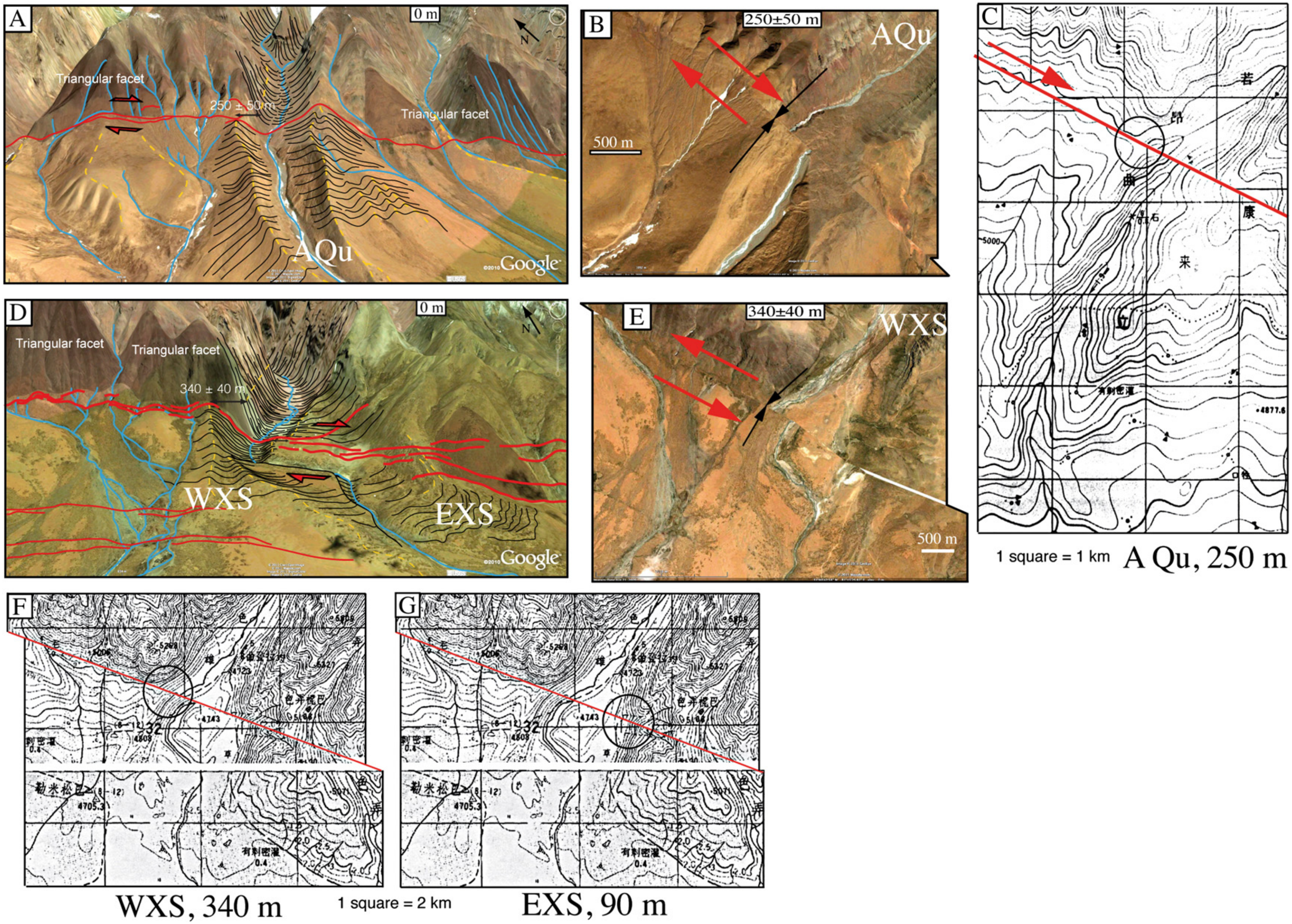

Fig. 14. Offset reconstruction at A Qu and WXS. (A) 3D view of the A Qu moraine today. (B) Reconstruction of the 250 ± 50 m offset of the A Qu western crest by the KRFF. (C) Reconstruction of the same A Qu moraine crest on the 1/50,000 topographic map. (D) 3D view of the West Xiong Se moraine today. (E) Reconstruction of the 340 ± 40 m offset of the West Xiong Se moraine crest by the KRFF. (F) Reconstruction of the same WXS moraine crest on the 1/100,000 topographic map. (G) Reconstruction of the 90 ± 40 m offset of the EXS moraine crest on the 1/100,000 topographic map.

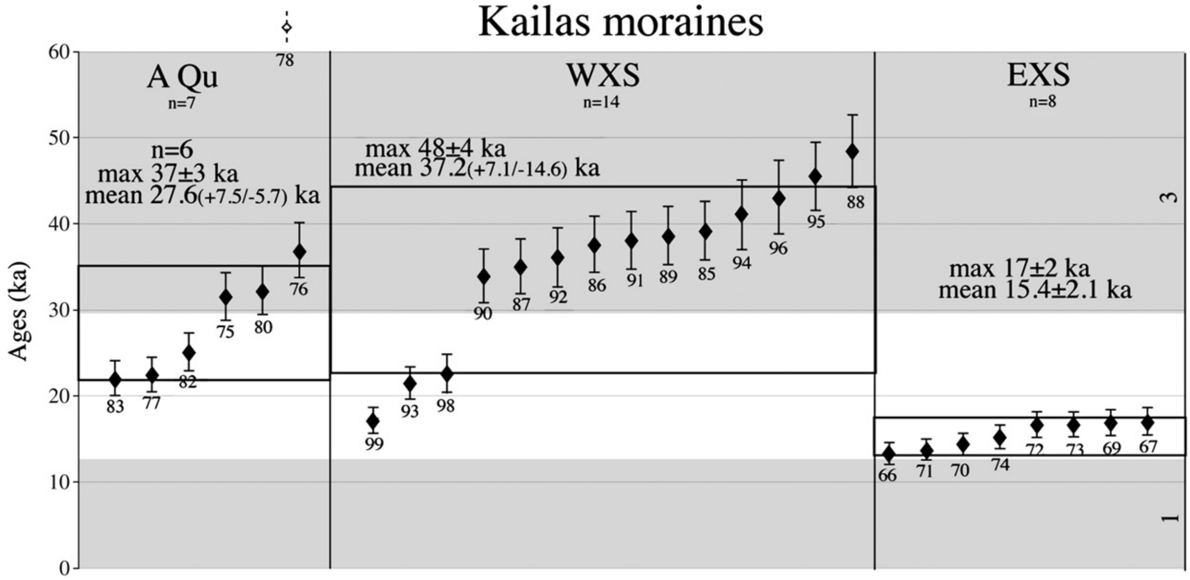

Fig. 15. Ages of the Kailas moraines. We distinguished two scenarios with "max" referring to the oldest age on the surface (outlier #78 on A Qu excluded) and "mean" referring to the median age of the surface. The gray-shaded sectors are the Marine Isotope Stages (MIS) of Imbrie et al. (1984) with the corresponding periods presented by the numbers on the right.

detail in Chevalier et al. (2011a) (see Section 3.1.5, Figs. 9 and S27) and Owen et al. (2010).

4.5.2. Offsets

Similar to what we observe at the Rengongpu site further north, prominent, active normal faults follow the steeper base of the range-front, which is composed of huge (~1600 m high), shallower-dipping (~20°) triangular facets capped by the mylonites of the Gurla Mandhata detachment (Murphy et al., 2002) (Figs. 2 and 17A). However hard to constrain, there is evidence for right-lateral movement at the Rongguo site. Two of the segments of the range-front fault zone that strike NW–SE, including the segment at and south of Rongguo, show spectacular en echelon faulting, with multiple, left-stepping, N to NNW-trending normal fault scarps (Fig. 20), indicative of a right-lateral component of slip, consistent with the regional, ~EW extensional regime. Also, at a more detailed level, the inner wall of M2/M1W appears to be right-laterally offset by an uncertain value of about 100–200 m across the fault zone (Fig. 21). However, estimates of the vertical offsets are uncertain because incision by the rills across M makes it impossible to define piercing points

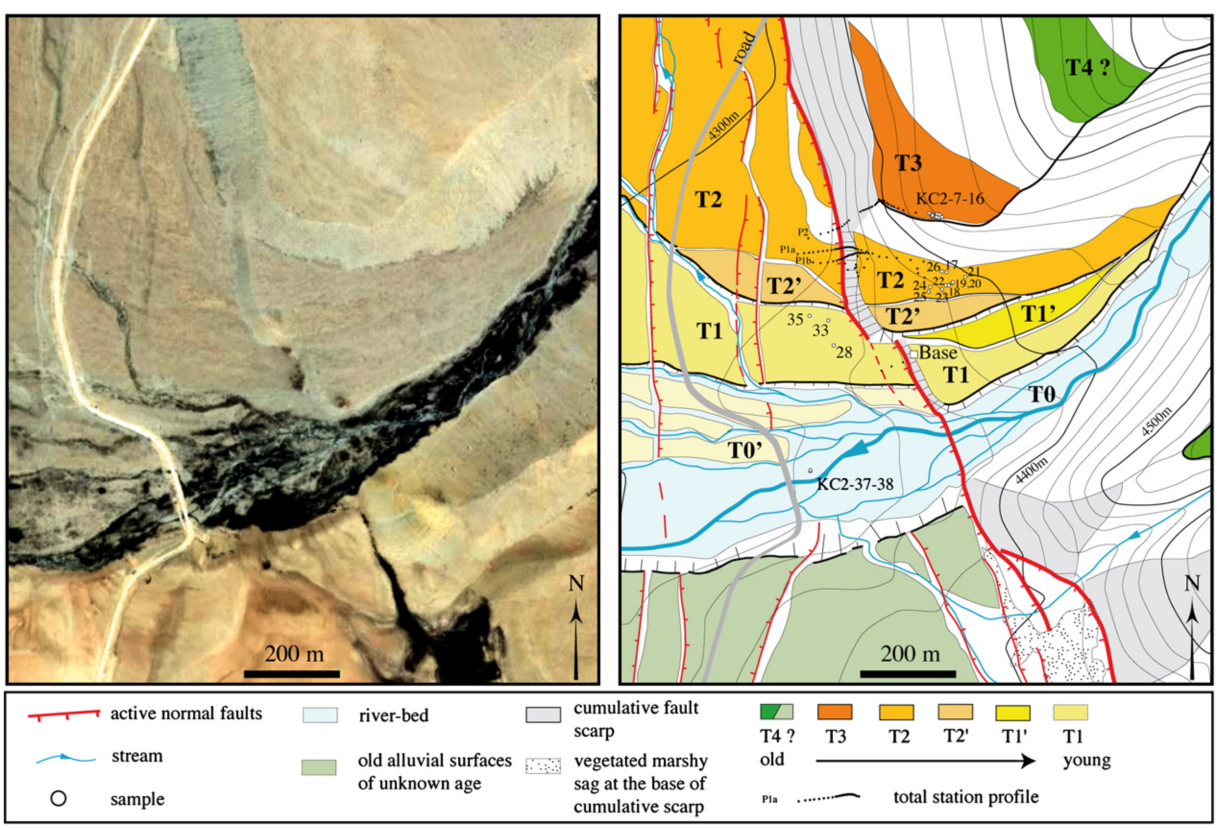

Fig. 16. Quickbird satellite image (2005) interpretation of the Rengongpu site (Site 5). Total station points (described in Fig. 18) are also plotted. Topographic contours every 20 m.

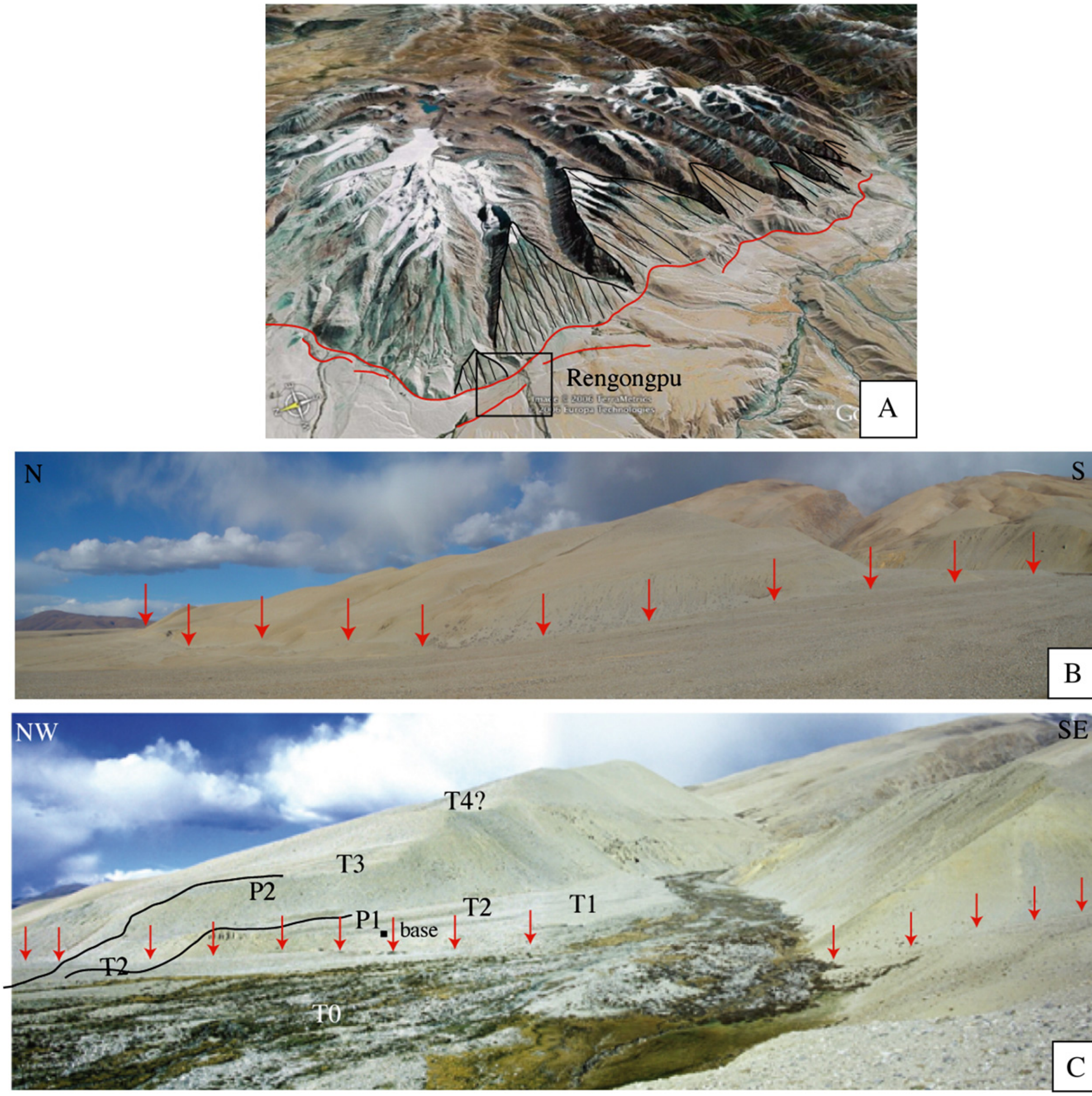

Fig. 17. Field photos of the Rengongpu site. (A) Google Earth image of the Gurla Mandhata area with huge triangular facets along the Gurla Mandhata detachment fault. (B) Field photo with red arrows showing the fault trace. (C) Close-up of the Rengongpu terraces where P1 and P2 refer to the two profiles made across the fault and described in Fig. 18.

at the fault. The profiles in Fig. 22B (obtained from the 1/50,000 topographic maps) show the moraine slopes and heights.

4.5.3. Surface ages

Eighteen samples were collected on the Rongguo crests: 3 on M1W (KC2-39-44), 6 on M1E (KC2-45-50), and 9 on M2 (KC2-51-59) (Fig. 20 and Table S1 here and in Chevalier et al., 2011a). Fig. 23 shows the ages of the Rongguo samples. M2 emplacement age may be taken as the average age of the 9 samples collected, $60.8^{+24.4}/_{-30.6}$ ka, while the oldest age is 95 ± 8 ka. As discussed in Chevalier et al. (2011a), and according to Owen et al. (2010), M1E and M1W are probably the same moraine with its oldest age being 45 ± 4 ka and its average age being $24.3^{+15.7}/_{-4.9}$ ka. The oldest age taken for M1 (45 ± 4 ka) would be roughly consistent with an emplacement during the penultimate coldest period of the last glacial cycle (late MIS-3, ~40 ka). A correlation with the climatic proxy curve for M2 is not as straightforward, but could coincide with the short glacials during MIS-5.

5. Slip-rate determination

5.1. Site 1: Menshi

Bounds on the right-lateral slip-rate along the Kailas Range Front fault (KRFF) and West Darchen fault (DF) at the Menshi site may be derived from the measured offsets and the cosmogenic surface exposure ages (blue in Fig. 24). If the smaller, best constrained offset (118 ± 18 m) is associated with T1 emplacement age ($24.1^{+11.3}/_{-5.1}$ ka), a median slip-rate of $4.7^{+1.8}/_{-1.4}$ mm/yr is obtained. Similarly, one could consider matching the maximum 430 ± 30 m offset with the poorly constrained T3 emplacement age ($107.6^{+29.7}/_{-37.6}$ ka) and derive a slip-rate of $4.0^{+2.2}/_{-0.9}$ mm/yr, which is similar to the rate defined by T1 average age and offset. However, we have less confidence in the

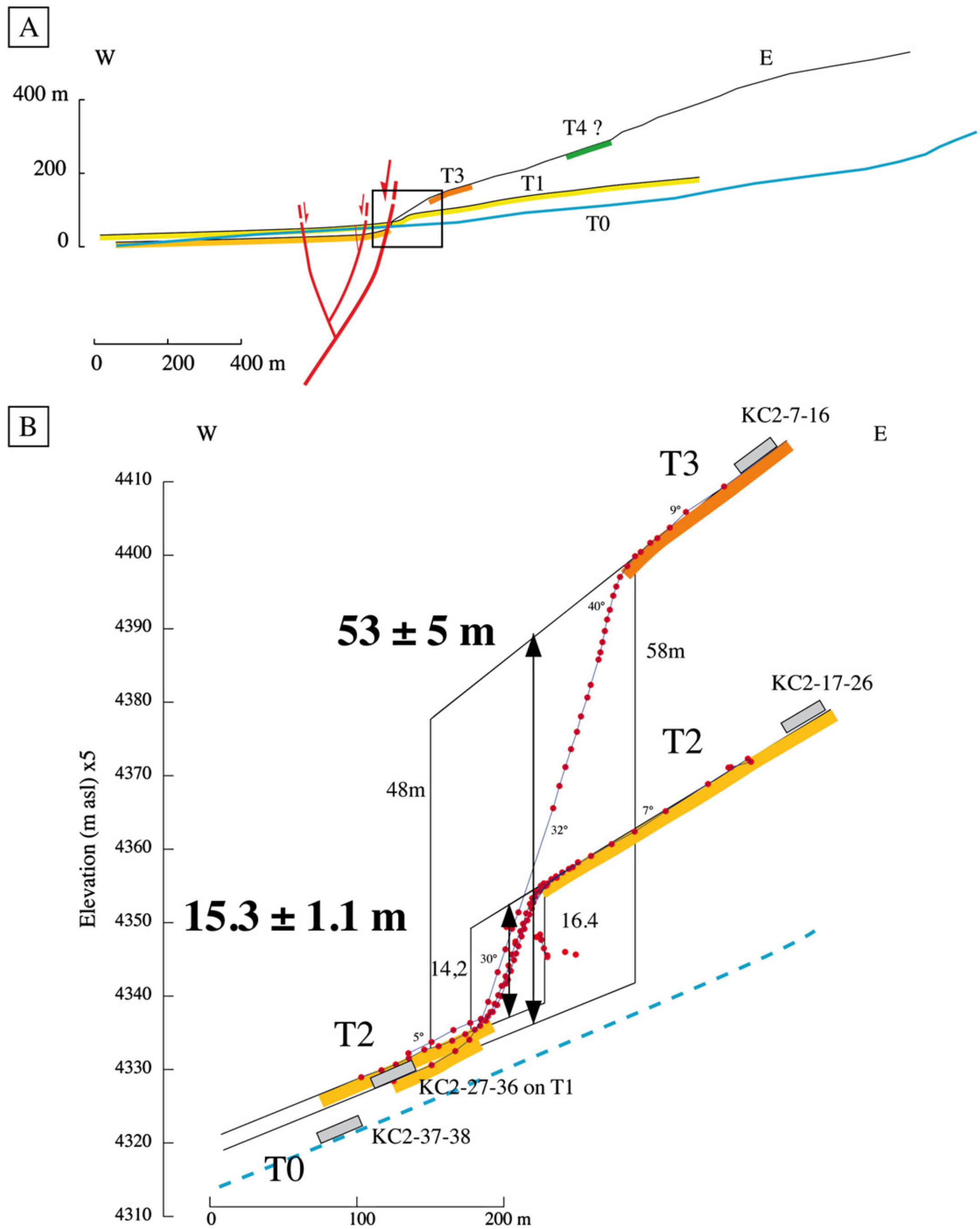

Fig. 18. Topographic cross-sections at Rengongpu site. (A) Topographic cross-sections at Rengongpu site from 1/50,000 scale topographic map with possible geometry of normal faults at depth. Terraces T1 to T4 are uplifted due to movement on the normal fault at the foot of the steep slope of Gurla Mandhata. Black rectangle is location of (B). (B) Detailed total station profiles (red dots) across main normal fault scarps and T2 and T3 terrace levels. Terrace slopes flatten from 7 to 9° east of the fault to about 5° west of it. Vertical offset of T2 and T3 is best estimated as average of vertical distance between sloping surfaces on either side of fault scarp and are about 15 and 53 m, respectively. Gray rectangles locate approximate position of sampling areas on each terrace level.

latter and consider the former as the most likely slip-rate along the KRFF at Menshi. The average slip-rate considering both offsets is $4.4^{+2.8}/_{-1.7}$ mm/yr. The age related to the 188 ± 18 m offset by the other prominent fault branch (DF) is bounded by the upper T2, of unknown age. We therefore use a "boxcar" age (Zechar and Frankel, 2009) of 19 ka (T1 minimum age) to 137.3 ka (T3 maximum age), yielding a slip-rate of $2.4^{+2.6}/_{-0.8}$ mm/yr along the DF at Menshi (Table 4).

Although additional data are required to more tightly constrain these velocities (such as on the glacial outwash and on the eastern fan), our results imply a net dextral slip-rate on order of at least $7.1^{+3.2}/_{-1.7}$ mm/yr, calculated by summing the slip-rate obtained from the two main fault branches (KRFF and DF) (Fig. 25). As elsewhere, minor slip on other smaller strands could add an additional few mm/yr to this estimate.

5.2. Site 2: La Zhi Tang

Bounds on the right-lateral slip-rate along the Darchen fault (DF) at the La Zhi Tang site may be derived from the measured offsets and the cosmogenic surface exposure ages (Table 4 and red in Fig. 24). Fluvial terraces in glaciated regions provide quantifiable records of climatic and tectonic changes, visible today as offset channels

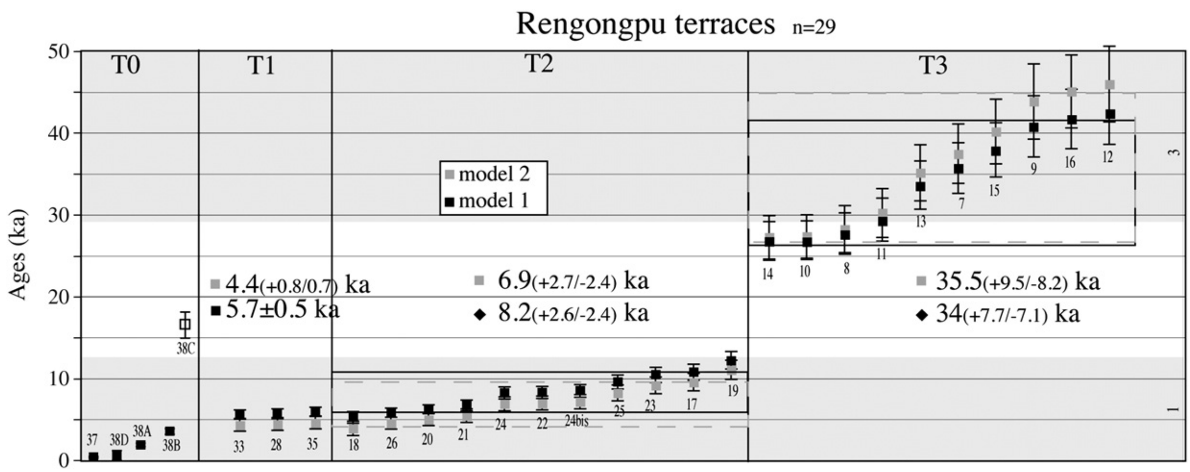

Fig. 19. Ages of the Rengongpu terraces. Same as in caption in Fig. 7 but with Model 2 ages referring to ages calculated with erosion and inheritance from T0 subtracted.

or risers. The ability of a stream to entrain sediments and incise its channel is sensitive to climatic and tectonic influences: a reduction of sediment load or an increase in stream power will cause the stream to incise its channel, leaving behind the former stream bed as a terrace (Whipple and Tucker, 1999). Determining fault slip-rates from dated, offset, fluvial terrace risers requires identification of equivalent piercing points on opposite sides of the fault (Gold et al., 2011). The offset risers are bounded by upper and lower terrace surfaces. This setting provides a particularly useful tool for reconstructing lateral slip-rates along a strike-slip fault due to their linearity on each side of the fault. For most fluvial systems, it is likely that some lateral refreshment occurs synchronously with riser displacement, thus yielding the age of the offset riser to be intermediate between the upper and lower surface abandonment ages. Therefore, here, we use the conservative approach of dating the abandonment age of both surfaces to bracket the age of the riser (e.g. Cowgill, 2007; Cowgill et al., 2009; Gold et al., 2009; Meriaux et al., 2005). The upper terrace age provides a maximum age for the riser, which could not have formed prior to incision and abandonment of the upper surface, while the lower terrace age provides a minimum age for the riser because after incision and abandonment of the lower terrace, its riser cannot have been modified by lateral erosion.

The smallest offset (7 ± 1 m) of the T1/T0′ riser can be matched with the age of T1 ($10.5^{+1.8}/{-}_{1.3}$ ka), yielding a minimum slip-rate of 0.7 ± 0.1 mm/yr. The 10 ± 1 m offset of the small channel on T1 can also be matched with the age of T1, yielding a slip-rate of 0.9 ± 0.2 mm/yr. The T1/T1′ riser offset of 18 ± 2 m is tightly bounded by the age of the lower terrace T1 and the age of the upper terrace T1′ ($10.5^{+1.8}/_{-1.3}$ and $11.1^{+1.2}/_{-1.4}$ ka, respectively, i.e. a boxcar of 9.2 to 12.3 ka), resulting in a slip-rate of $1.7^{+0.3}/_{-0.2}$ mm/yr. Matching the maximum T1′/T1″ 24 ± 2 m offset with T1′ and T1″ ages ($11.1^{+1.2}/_{-1.4}$ and $12.3^{+1.4}/_{-1.3}$ ka, respectively, i.e. a boxcar of 9.7 to 13.7 ka) yields a maximum slip-rate of 2.1 ± 0.3 mm/yr. The T2/T1′ minimum offset of 80 ± 20 m may constrain a slip-rate of $2.2^{+2.0}/_{-0.8}$ mm/yr considering the age of the lower terrace T1″ ($12.3^{+1.4}/_{-1.3}$ ka) and the age of the higher terrace T2 ($49.9^{+12.6}/_{-9.0}$ ka) (i.e. a boxcar of 11 to 62.5 ka). The average rate on the DF at La Zhi Tang is $1.5^{+2.1}/_{-0.9}$ mm/yr, which is slightly slower, but on the order of what we obtained along the DF at Menshi ($2.4^{+2.6}/_{-0.8}$ mm/yr).

Concerning the undated Tu Qiong moraine (crossing the KRFF) upstream from LZT, matching its 270 ± 30 m offset (similar to the neighboring A Qu moraine offset, see below) with the age of the A Qu moraine (oldest age 37 ka, mean age ~28 ka, or simply with MIS-3 age, ~40 ka), would yield a slip-rate of ~7 mm/yr, slightly higher than what we found at Menshi (~5 mm/yr) along the KRFF but similar to what we find further east, as described below.

5.3. Sites 3 and 4: A Qu, West and East Xiong Se moraines

Bounds on the right-lateral slip-rate along the Kailas Range Front fault (KRFF) at the Kailas moraines are best estimated from the offsets and the cosmogenic surface exposure ages (Table 4 and green in Fig. 24) of the A Qu, West and East Xiong Se moraines south of the fault, relative to the edge of glacial incision north of the fault, as at other comparable glacial sites (Qilian Shan, Lasserre et al., 2002; Manikala, Chevalier et al., 2005a).

Assuming that the 250 ± 50 m offset of the A Qu moraine accrued after its emplacement (oldest age 37 ± 3 ka, mean age $27.6^{+7.5}/_{-5.7}$ ka) yields a slip-rate of $6.8^{+1.5}/_{-1.4}$ or $8.9^{+3.2}/_{-2.4}$ mm/yr, respectively. For the West Xiong Se moraine, a similar rate is obtained using the same hypothesis: a 340 ± 40 m offset accrued over 48 ± 4 ka (oldest age) or $37.2^{+7.1}/_{-14.6}$ ka (mean age), yields a slip-rate of $7.0^{+1.1}/_{-1.0}$ or $9.2^{+5.5}/_{-1.8}$ mm/yr, respectively. Finally, matching the 90 ± 40 m offset of the East Xiong Se moraine with its emplacement age (oldest age 17 ± 2 ka or mean age 15.4 ± 2.1 ka), yields a slip-rate of $5.3^{+2.5}/_{-2.4}$ or $5.8^{+2.8}/_{-2.6}$ mm/yr, respectively. The average slip-rate on the KRFF at the Kailas moraines (Tu Qiong is not included because it is not dated) is thus $6.4^{+2.4}/_{-2.3}$ mm/yr (oldest ages) or $8.0^{+7.0}/_{-4.0}$ mm/yr (mean ages).

The total slip-rate across the Karakorum fault system just west of Mount Kailas should thus be the sum of the rate on the KRFF at the Kailas moraines and the rate on the DF at La Zhi Tang site, i.e. $7.9^{+3.2}/_{-2.5}$ mm/yr (if oldest ages) or $9.5^{+7.3}/_{-4.1}$ mm/yr (if mean ages) (Table 4). This rate appears slightly faster, but within uncertainties, than further west, at Menshi (~7 mm/yr). As elsewhere, minor slip on other smaller strands to the south, and the vertical component of throw, could add an additional few mm/yr to this estimate.

5.4. Sites 5 and 6: Pulan graben

Bounds on the slip-rate along the mainly normal fault that follows the east side of the Pulan half-graben may be derived from the measured offsets and the cosmogenic surface exposure ages (Table 4) at the Rengongpu terraces. Matching the 15.3 ± 1.1 m offset of T2E/T2W with T2 age ($8.2^{+2.6}/_{-2.4}$ ka) yields a vertical slip-rate of $1.9^{+0.8}/_{-0.5}$ mm/yr. Matching the 53 ± 5 m minimum offset of T3/T2W with T3 age ($34.0^{+7.7}/_{-7.1}$ ka) yields a minimum vertical slip-rate of $1.6^{+0.4}/_{-0.3}$ mm/yr.

6. Discussion

The first qualitative estimates of the Quaternary slip-rate on the Karakorum fault were proposed 15 years ago by Liu (1993), who

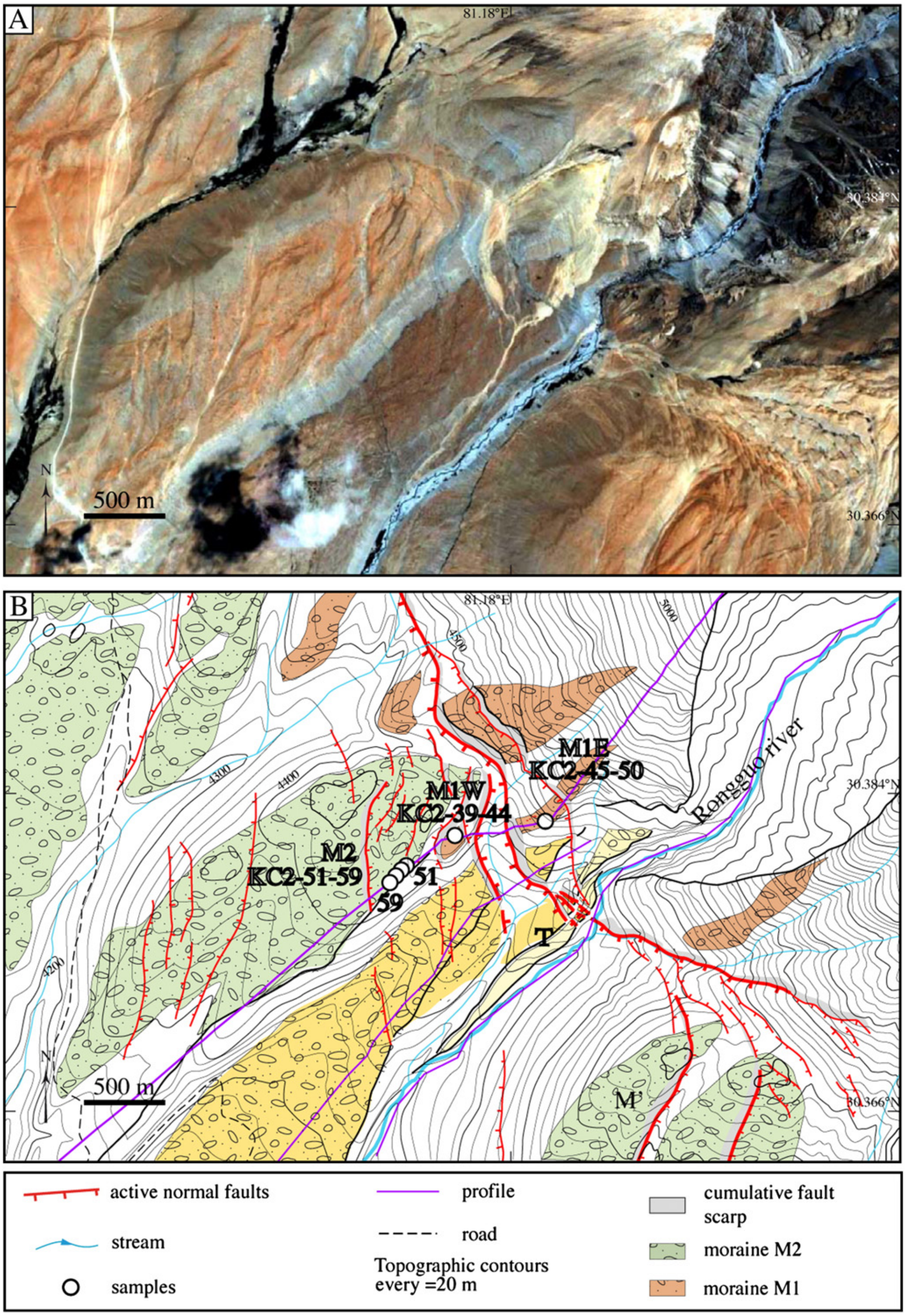

Fig. 20. Quickbird satellite image (2005) and interpretation of the Rongguo site (Site 6). En-echelon faulting on M′ (lower right corner), with multiple left-stepping, N to NNW-trending normal fault scarps, indicate a right-lateral component of slip, consistent with the regional, ~EW extensional regime.

briefly described some sites targeted in this study. Given the dearth of direct dating techniques at the time, Liu (1993)'s estimates were based on climatic inference, and on one cosmogenic ^{3}He age (8234 ± 668 a B.P., Staudacher et al., 1992) from a boulder collected on a "young" moraine facing the Gar River bridge. All of Liu (1993)'s estimates were higher (18–35 mm/yr) than the currently published slip-rate range (0–11 mm/yr) (geodetic: Banerjee and Burgmann, 2002; Chen et al., 2004; Jade et al., 2004, 2010; Loveless and Meade, 2011; Styron et al., 2011; Wang et al., 2011; Wright et al., 2004; short-term geologic: Brown et al., 2002; Chevalier et al., 2005a, 2011b; long-term geologic: England and Molnar, 2005; Lacassin et al., 2004; Phillips and Searle, 2007; Phillips et al., 2004; Robinson, 2009a, 2009b; Rutter et al., 2007; Valli et al., 2007, 2008; Wang et al., 2009). It is now clear why this was the case. The fans at Menshi for instance appear to be at least twice as old as the age values inferred by Liu (1993) (10–12 ka). Similarly, while (most likely) LGM moraines exist in most of the glacial catchments we sampled, it appears to be the MIS-3 moraines (~40 ka), again about twice as old as the LGM moraines (~20 ka), that reach farthest out from the range-front, and thus are in several cases the norm with which to measure

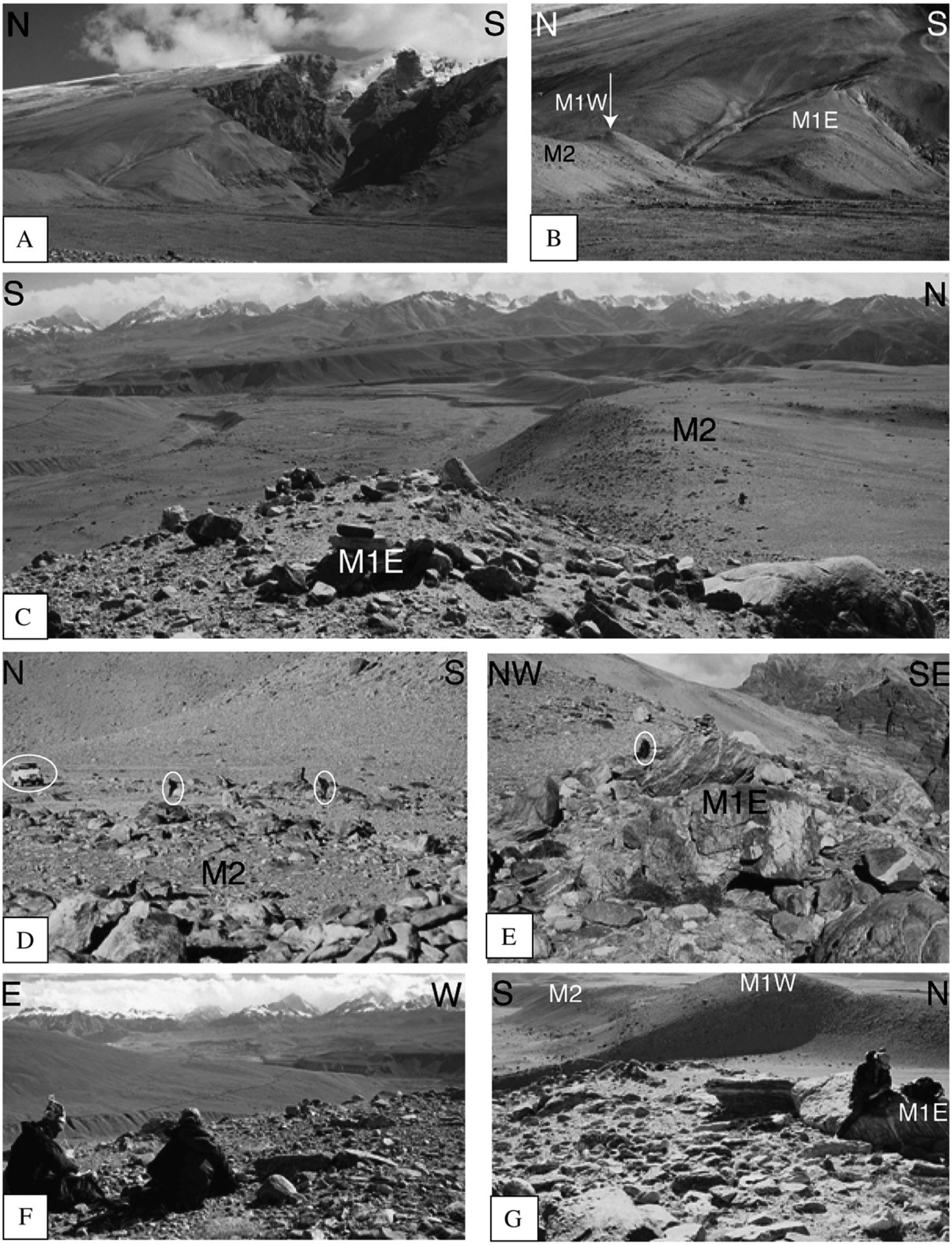

Fig. 21. Field photos of the Rongguo moraines in the Pulan graben, from Chevalier et al. (2011a). The possible 100–200 m right-lateral offset of the moraine crest is visible on (A), (B), (C) and (G). The deeply entrenched Rongguo valley is visible on (A). Panels (C) to (G) depict the moraine surface textures. White circles on (D) and (E) show people and car, for scale.

the slip-rate where they are offset by range-front branches of the fault.

Though not exhaustive, our results provide the most comprehensive set of quantitative geomorphic constraints on the slip-rate across the southern stretch of the Karakorum fault zone between the 30° bend at Baer and the Mount Kailas–Pulan graben, i.e. along the Menshi–Kailas basin, to date. Our final estimates of the most plausible values of the slip-rates at the 4 sites along the KF described in this paper are

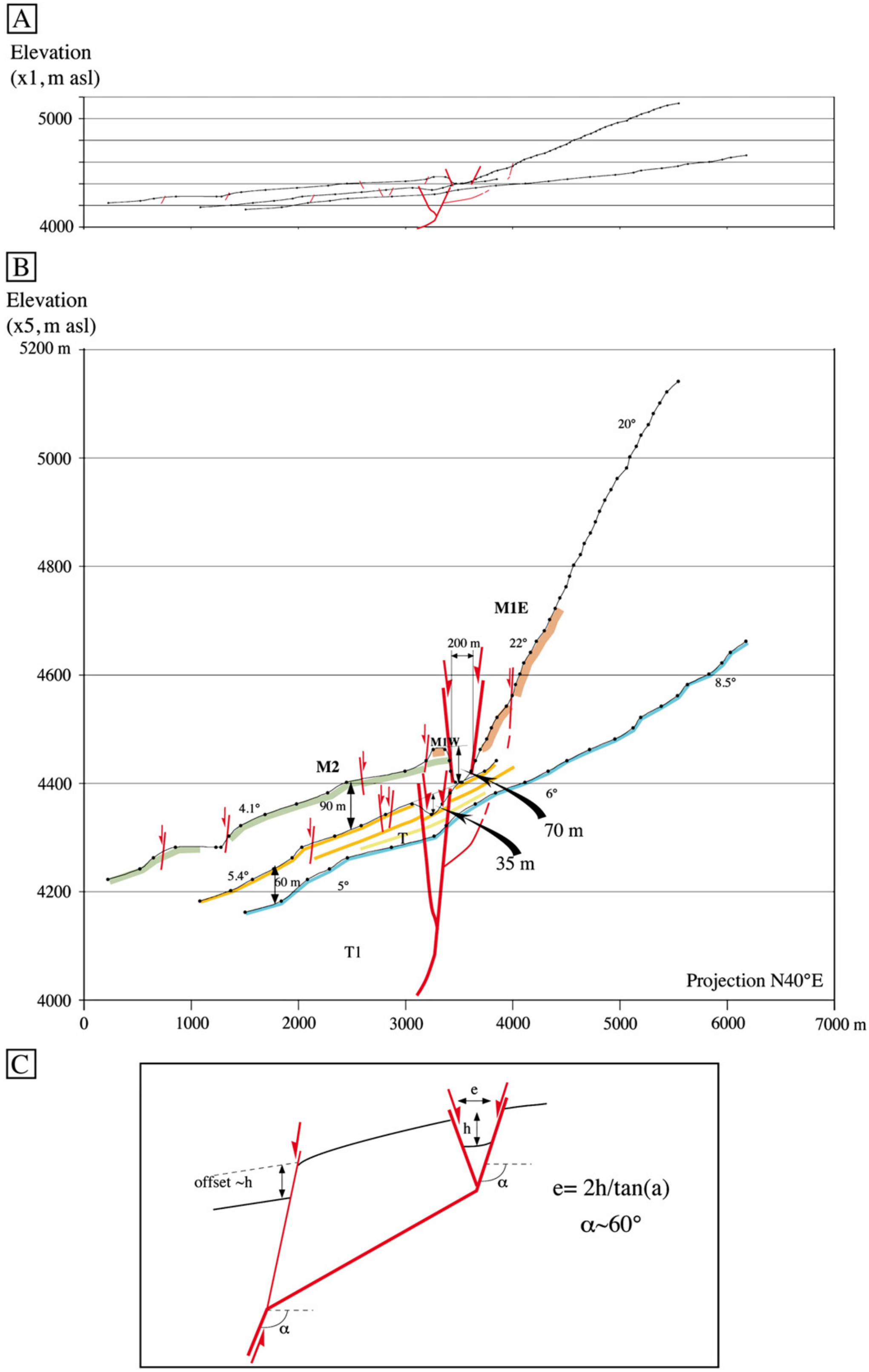

Fig. 22. Topographic cross-sections at Rongguo site. (A,B) Topographic cross-sections at Rengongpu site from 1/50,000 scale topographic map with possible geometry of normal faults at depth. (C) Moraine slopes flatten from 20° to 22° east of the fault to about 4–5° west of it. Vertical and horizontal offsets of M1 are unclear due to the presence of several fault strands and channels destroying evidences.

summarized in Fig. 25 and Table 4. Just north of Baer, along the Manikala range-front fault, it is >5–11 mm/yr (Chevalier et al., 2005a, 2005b) over an age range of 20 to 180 ka, across one branch of the fault. South of Baer (Fig. 1), the dextral slip-rate on two of several fault branches observed in the Menshi–Kailas basin, measured over a ~200 ka range, appears to be similar at $7.1^{+3.2}/_{-1.7}$ mm/yr (Menshi KRFF + DF), and $7.9^{+3.2}/_{-2.5}$ to $9.5^{+7.3}/_{-4.1}$ mm/yr (Kailas KRFF + La Zhi Tang DF, oldest or mean moraine age, respectively).

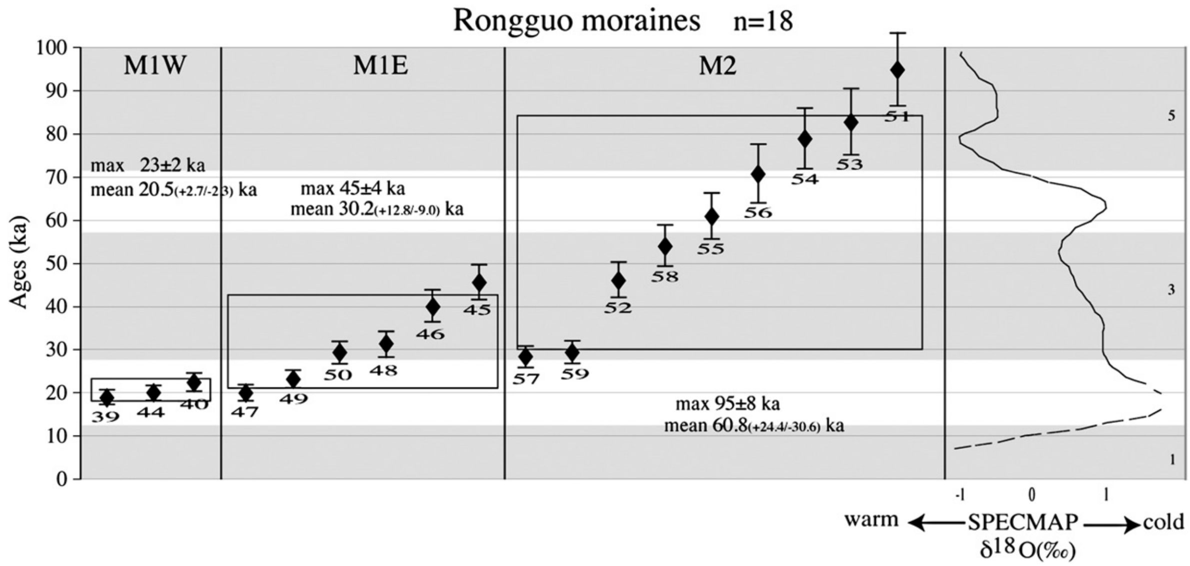

Fig. 23. Ages of the Rongguo moraines. Same as in caption in Fig. 15.

The rates we obtain for the southern segment of the KF appear to be fast and constant between Manikala and the Kailas area (~200 km). This is in contradiction with the inference from other studies (e.g. Murphy et al., 2000; Phillips et al., 2004; Robinson, 2009a; Searle et al., 1998; Styron et al., 2011; Valli et al., 2008) indicating that the rate (and magnitude of offset) might be decreasing, like what is observed along the Altyn Tagh fault (e.g. Meriaux et al., 2005; Meyer et al., 1996; Zhang et al., 2007). This important finding may therefore refute the idea that the KF ends at the Kailas (e.g. Murphy et al., 2002; Ratschbacher et al., 1994) and may however imply an eastward continuation along the Yarlung–Zangbo suture (Lacassin et al., 2004; Peltzer and Tapponnier, 1988), a southwestward continuation along the Gurla Mandhata–Humla fault system in the Pulan graben and into Nepal (e.g. Armijo et al., 1989; Chen et al., 2004; Lacassin et al., 2004; Murphy and Copeland, 2005; Styron et al., 2011), as well as a possible northward transfer along the Gangdese Range along the Karakorum–Jiali fault zone (Armijo et al., 1989). Indeed, recent geodetic studies estimate a right-lateral slip-rate of 2.8 ± 0.8 mm/yr (Chen et al., 2004) to 5.5 ± 0.4 – 9.8 ± 0.4 mm/yr (Loveless and Meade, 2011) along the Yarlung Zangbo suture. In addition, the minimum, vertical slip-rate of $1.6^{+0.4}/_{-0.3}$ mm/yr we found in Pulan (for the last ~40 ka), is on the order of that obtained from other southern Tibet grabens, such as the Ama Drime graben (exhumation rate ~1 mm/yr, Jessup et al., 2008; Kali et al., 2010) and the Yadong–Gulu graben (minimum average rate of 1.9 ± 0.6 mm/yr, Armijo et al., 1986), as well as a preliminary late Quaternary rate obtained from the Ashkule graben in Northwest Tibet (1–2 mm/yr, Haibing Li, pers. Comm.). To this vertical rate, we should add a dextral rate along the Gurla Mandhata detachment fault as well as along the Humla–Tibrikot faults in Nepal (maybe several mm/yr, Styron et al., 2011).

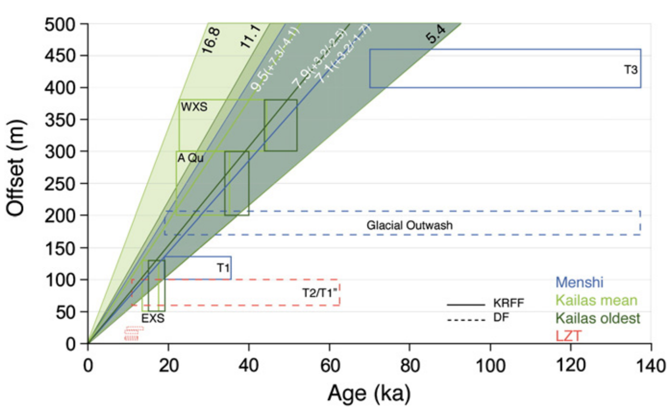

Fig. 24. Late Quaternary slip-rates summary. Offsets vs. ages plot (1-sigma, Model 1) with average slip-rates determined for each site along the KF (Pulan sites not included). The rates determined along the Darchen fault (DF) (dashed boxes) must be added to those determined along the Kailas Range-Front fault (KRFF) (continuous boxes) to obtain the total slip-rate along the two branches. Light and dark green colors refer to the Kailas moraine mean and oldest ages, respectively.

Outside the region we studied, the other slip-rate values obtained with the same technique, northwest of Bangong Lake (4 ± 1 mm/yr, Brown et al., 2002) and in the Muji–Tashkorgan basin (>4.5 mm/yr along the Muji fault only and possibly >9 mm/yr across the KF system, Chevalier et al., 2011b), are comparable to what we determined along a single branch of the fault (KRFF) at Gar (Chevalier et al., 2005a) and Menshi (Fig. 25). Brown et al., (2002)'s rate might become identical to our net slip-rate along the two main branches of the fault if they also targeted both main branches of the fault in the area.

The comparison between our morphochronological, Quaternary slip-rates and the InSAR and geodetic rates available to date (Fig. 25) shows that the latter two fall mostly short of the long-term rates we find. Chevalier et al. (2005a) argued that this might be due to real, centennial slip-rate variations, as a result of the very different time-spans sampled by the techniques used: ~10 years for GPS and InSAR, and ~200 ka for Quaternary slip-rate studies (e.g. this study and Chevalier et al., 2005a). Other reasons however, might be invoked. The low InSAR rate of Wright et al. (2004), for instance (1 ± 3 mm/yr, Fig. 25) may result from the fact that these authors dismissed the effect of tropospheric biases, which have been shown to be significant along the northern edge of Tibet (Elliott et al., 2008), and quite difficult to correct. Also, in the study of Wright et al. (2004), the addition of InSAR pairs increases considerably the noise in the data (see Supplementary material in Wright et al., 2004) rather than the signal, making it impossible to reach a sound interpretation: the Karakorum fault is not left-lateral. Nor is it barely visible in the landscape, whether in the field or on many extant images. Concerning the two extant GPS studies, which show markedly disparate results, one is consistent with our average long-term value (Banerjee and Burgmann, 2002; 11 ± 4 mm/yr), and

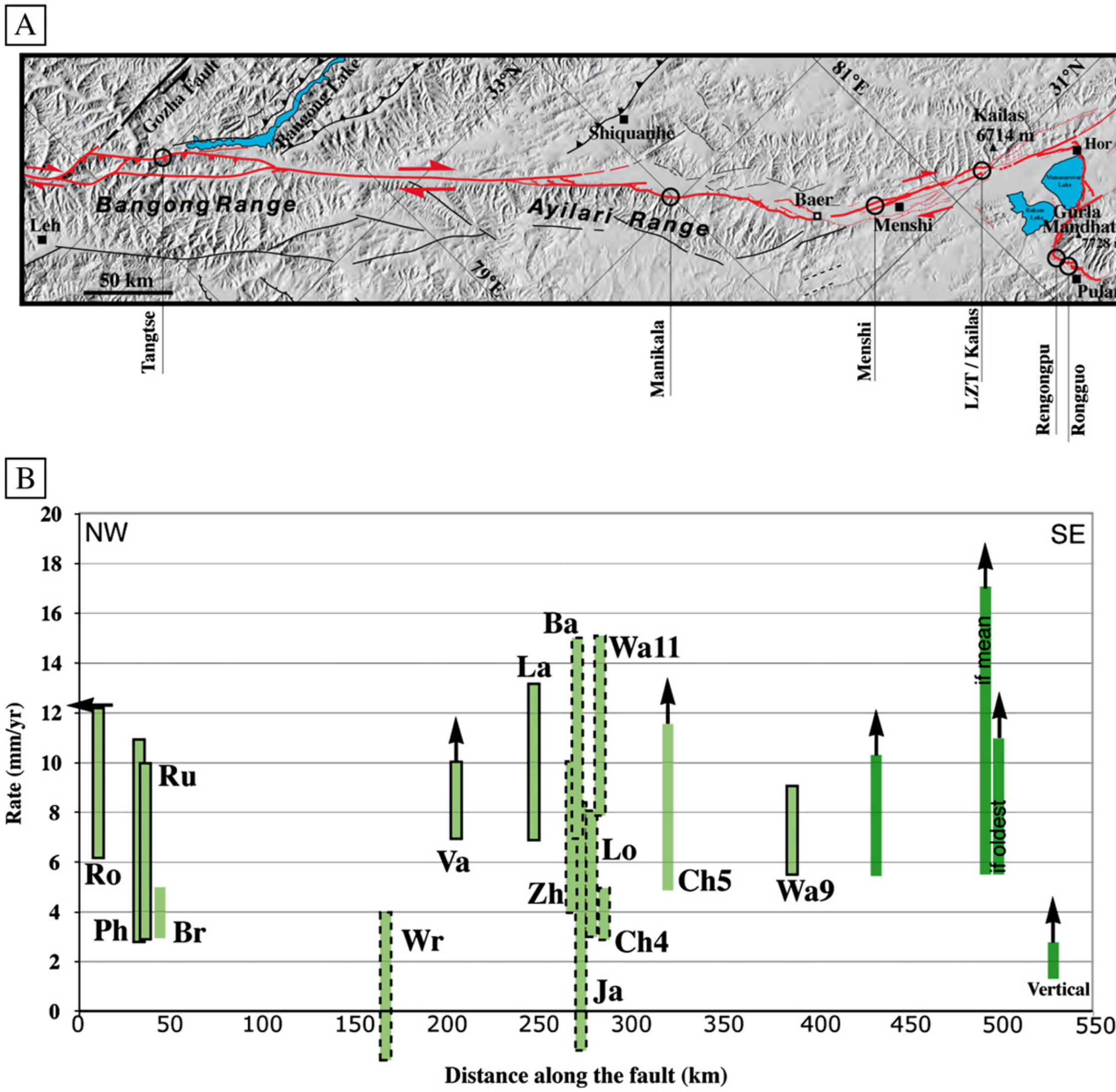

Fig. 25. Slip-rates on the Karakorum fault. Slip-rates on the KF from Bangong Lake to the Kailas, determined with several methods over several timescales. Dashed green boxes refer to geodetic studies, green boxes with black outline refer to long-term geologic studies, while light green boxes refer to Quaternary slip-rate studies. "If mean" refers to the rate calculated using the mean Kailas moraine ages while "if oldest" is calculated using the oldest moraine ages. Br = Brown et al. (2002): 4 ± 1 mm/yr, Ba = Banerjee and Burgmann (2002): 11 ± 4 mm/yr, Ch4 = Chen et al. (2004): 4 ± 1 mm/yr, Ch5 = Chevalier et al. (2005a): 5.5 ± 0.5 – 10.7 ± 0.7 mm/yr, Ja = Jade et al. (2004, 2010): 3 – 3.4 ± 5 mm/yr, La = Lacassin et al. (2004): 10 ± 3 mm/yr, Lo = Loveless and Meade (2011): 3 ± 0.1 – 8 mm/yr, Ph = Phillips et al. (2004, 2007): 2.7 – 10.2 mm/yr, Ro = Robinson (2009a): 6.89 ± 0.8 – 10.8 ± 1.3 mm/yr, Ru = Rutter et al. (2007): 3 – 10 mm/yr, Va = Valli et al. (2007): > 8.5 ± 1.5 mm/yr, Wa9 = Wang et al. (2009): 7.3 ± 1.8 mm/yr, Wa11 = Wang et al. (2011): 11.6 ± 3.7 mm/yr, Wr = Wright et al. (2004): 1 ± 3 mm/yr, Zh = Zhang et al. (2004): 7 ± 3 mm/yr.

the other is less than our lower bounds at Manikala and Menshi (Jade et al., 2004, 2010; ~3 mm/yr), technical shortcomings can also be the cause. Perhaps the most important one is that station positions in the second studies are quite close to the fault, in fact within the elastic deformation zone expected in a region of thickened crust. In addition, in both studies, only one GPS station (SHIQuanhe) exists north of the fault, close to the Karakorum fault system and local branches of the Jiali–Karakorum fault zone. Also, it has recently been argued that low GPS values of slip-rates could be unreliable, not because of geodetic measurements themselves but because of the way they are extrapolated in time to obtain long-term slip-rates (using a too-high effective friction coefficient, while it should be < 0.1) (He and Chery, 2008). Lastly, it is worth noticing that, even though the KF is one of the major active faults in Central Asia, its recorded seismic activity has been quite low for at least the past 35 years, for earthquakes with M > 5. This could explain why the GPS/InSAR rates are slow, since they are measured on a ~10 year timescale.

7. Conclusions

(1) By investigating 2 fluvial and 3 moraine sites along the two main branches (Kailas Range Front and Darchen faults) of the Karakorum fault, with a total of 12 markers that are offset by up to 430 ± 30 m, spanning ~200 ka, we determined a slip-rate of > 7–8 mm/yr along the southernmost segment of the KF. This rate is very similar to what we previously found at Manikala along one branch of the fault (> 5.5 ± 0.5 – 10.7 ± 0.7 mm/yr) and therefore appears to be constant along the southern ~200 km of the fault. This rate lies within the currently published range of slip-rates (0–11 mm/yr), including geodetic, short-term geologic (up to several ka) and long-term geologic (Ma), however toward the higher end.

(2) The fact that the slip-rate does not decrease toward the east but remains relatively constant implies that the Karakorum fault does not terminate at the Kailas region, but instead

continues eastward along the Yarlung Zangbo suture, as well as southwestward along the Gurla Mandhata–Humla fault system, or even possibly northward along the Gangdese Range and the Karakorum–Jiali fault zone.

While the results of our study provide the most robust quantitative data on the Karakorum fault slip-rate to date, improved geodetic and InSAR results are warranted as are additional dated offset geomorphic markers.

Acknowledgments

This work was performed under the auspices of the U.S. Department of Energy by the University of California, Lawrence Livermore National Laboratory; also supported by INSU and CNRS (Paris, France). This study was also financially supported by the China Geological Survey (project #1212011121267) and the Basic Outlay of Scientific Research Work from the Ministry of Science and Technology, China (#J1126). We thank K. Blisniuk and E. Shelef for their informal help, as well as A. Matmon and R. Bendick for their review on a much earlier version of this manuscript. We also thank two anonymous reviewers for their thorough and constructive reviews on this manuscript.

Appendix A. Supplementary Data

Supplementary data associated with this article can be found in the online version, at doi:10.1016/j.tecto.2011.12.014. These data include Google maps of the most important areas described in this article.

References

Armijo, R., Tapponnier, P., Mercier, J., Tonglin, H., 1986. Quaternary extension in southern Tibet: field observations and tectonic implications. Journal of Geophysical Research 91, 13,803–13,872.

Armijo, R., Tapponnier, P., Tonglin, H., 1989. Late Cenozoic right-lateral strike-slip faulting in southern Tibet. Journal of Geophysical Research 94 (B3), 2787–2838. doi:10.1029/JB091iB14p13803.

Arnaud, N., Brunel, M., Cantagrel, J.M., Tapponnier, P., 1993. High cooling and denudation rates at Kongur Shan, eastern Pamir (Xinjiang, China) revealed by ^{40}Ar/^{39}Ar Alkali feldspar thermochronology. Tectonics 12, 1335–1346. doi:10.1029/93TC00767.

Avouac, J.-P., Tapponnier, P., 1993. Kinematic model of active deformation in central Asia. Geophysical Research Letters 20, 895–898. doi:10.1029/93GL00128.

Balco, G., Stone, J.O., Lifton, N.A., Dunai, T.J., 2008. A complete and easily accessible means of calculating surface exposure ages or erosion rates from ^{10}Be and ^{26}Al measurements. Quaternary Geochronology. doi:10.1016/j.quageo.2007.12.001.

Banerjee, P., Burgmann, R., 2002. Convergence across the northwest Himalaya from GPS measurements. Geophysical Research Letters 29 (13). doi:10.1029/2002GL015184 (art. no. 1652).

Bendick, R., Bilham, R., Freymueller, J., Larson, K., Yin, G., 2000. Geodetic evidence for a low slip rate in the Altyn Tagh fault system. Nature 404, 69–72. doi:10.1038/35003555.

Brown, E.T., Bendick, R., Bourles, D.L., Gaur, V., Molnar, P., Raisbeck, G.M., Yiou, F., 2002. Slip rates of the Karakorum fault, Ladakh, India, determined using cosmic ray exposure dating of debris flows and moraines. Journal of Geophysical Research 107. doi:10.1029/2000JB000100 (art. no. 2192).

Chen, Z., Burchfiel, B.C., Liu, Y., King, R.W., Royden, L.H., Tang, W., Wang, E., Zhao, J., Zhang, X., 2000. Global positioning system measurements from eastern Tibet and their implications for India/Eurasia intercontinental deformation. Journal of Geophysical Research 105 (B7), 16,215–16,227. doi:10.1029/2000JB900092.

Chen, Q., Freymueller, J.T., Yang, Z., Xu, C., Jiang, W., Wang, Q., Liu, J., 2004. Spatially variable extension in southern Tibet based on GPS measurements. Journal of Geophysical Research 109, B09401. doi:10.1029/2002JB00235.

Chevalier, M.-L., Ryerson, F.J., Tapponnier, P., Finkel, R.C., Van Der Woerd, J., Haibing, Li, Qing, Liu, 2005a. Slip-rate measurements on the Karakorum fault may imply secular variations in fault motion. Science 307, 411–414. doi:10.1126/science.1105466.

Chevalier, M.-L., Ryerson, F.J., Tapponnier, P., Finkel, R.C., Van Der Woerd, J., Haibing, Li, Qing, Liu, 2005b. Response to comment on "Slip-rate measurements on the Karakorum fault may imply secular variations in fault motion". Science 309, 1326c. doi:10.1126/science.1112629.

Chevalier, M.-L., Hilley, G., Tapponnier, P., Van Der Woerd, J., Liu-Zeng, J., Finkel, R.C., Ryerson, F.J., Li, H., Liu, X., 2011a. Constraints on the late Quaternary glaciations in Tibet from cosmogenic exposure ages of moraine surfaces. Quaternary Science Reviews 30, 528–554. doi:10.1016/j.quascirev.2010.11.005.

Chevalier, M.-L., Li, H., Pan, J., Pei, J., Wu, F., Xu, W., Sun, Z., Liu, D., 2011b. Fast slip-rate along the northern end of the Karakorum fault system, western Tibet. Geophysical Research Letters 38, L22309. doi:10.1029/2011GL049921.

Cowgill, E., 2007. Impact of riser reconstructions on estimation of secular variation in rates of strike-slip faulting: revisiting the Cherchen River site along the Altyn Tagh fault, NW China. Earth and Planetary Science Letters 254, 239–255. doi:10.1016/j.epsl.2006.09.015.

Cowgill, E., Gold, R.D., Chen, X., Wang, X.F., Arrowsmith, J.R., Southon, J., 2009. Low Quaternary slip rate reconciles geodetic and geologic rates along the Altyn Tagh fault, northwestern Tibet. Geology 37 (7), 647–650. doi:10.1130/G25623A.1.

Desilets, D., Zreda, M., 2003. Spatial and temporal distribution of secondary cosmic-ray nucleon intensities and applications to in-situ cosmogenic dating. Earth and Planetary Science Letters 206, 21–42. doi:10.1016/S0012-821X(02)01088-9.

Desilets, D., Zreda, M., Prabu, T., 2006. Extended scaling factors for in situ cosmogenic nuclides: new measurements at low latitude. Earth and Planetary Science Letters 246, 265–276. doi:10.1130/B26422.1.

Dunai, T., 2000. Scaling factors for production rates of in situ produced cosmogenic nuclides: a critical reevaluation. Earth and Planetary Science Letters 176, 157–169.

Dunai, T., 2001. Influence of secular variation of the magnetic field on production rates of in situ produced cosmogenic nuclides. Earth and Planetary Science Letters 193, 197–212. doi:10.1016/S0012-821X(01)00503-9.

Elliott, J.R., Biggs, J., Parsons, B., Wright, T.J., 2008. InSAR slip rate determination on the Altyn Tagh Fault, northern Tibet, in the presence of topographically correlated atmospheric delays. Geophysical Research Letters 35, L12309. doi:10.1029/2008GL033659.

England, P.C., Molnar, P., 1997. The field of crustal velocity in Asia calculated from quaternary rates of slip on faults. Geophysical Journal International 130, 551–582.

England, P.C., Molnar, P., 2005. Late Quaternary to decadal velocity fields in Asia. Journal of Geophysical Research 110, B12401. doi:10.1029/2004JB003541.

Flesch, L., Bendick, R., 2007. Present-day kinematics at the India-Asia collision zone: comment. Geology 36. doi:10.1130/G24443C.1.

Gasse, F., et al., 1991. A 13,000 year climate record from Western Tibet. Nature 353, 742–745.

Gold, R.D., Cowgill, E., Arrowsmith, J.R., Gosse, J., Chen, X., Wang, X.F., 2009. Riser diachroneity, lateral erosion, and uncertainty in rates of strike-slip faulting: a case study from Tuzidun along the Altyn Tagh fault, NW China. Journal of Geophysical Research 114, B04401. doi:10.1029/2008JB005913.

Gold, R.D., Cowgill, E., Arrowsmith, J.R., Chen, X., Sharp, W.D., Cooper, K.M., Wang, X.F., 2011. Faulted terrace risers place new constraints on the late Quaternary slip rate for the central Altyn Tagh fault, northwest Tibet. Geological Society of America Bulletin. doi:10.1130/B30207.1.

Gosse, J., Phillips, F., 2001. Terrestrial in situ cosmogenic nuclides: theory and application. Quaternary Science Reviews 20, 1475–1560.

Hanks, T.C., Thatcher, W., 2006. The slip-rate discrepancy for the Altyn Tagh fault: an example of epistemic uncertainty. Fall Meet. Suppl., Abstract T21E-03: Eos Trans. AGU, 87(52).

Harkins, N., Kirby, E., 2008. Fluvial terrace riser degradation and determination of slip rates on strike-slip faults: an example from the Kunlun fault, China. Geophysical Research Letters 35, L05406. doi:10.1029/2007GL033073.

Harkins, N., Kirby, E., Shi, X., Wang, E., Burbank, D., Fan, C., 2010. Millennial slip rates along the eastern Kunlun fault: implications for the dynamics of intracontinental deformation in Asia. Lithosphere 2 (4), 247–266. doi:10.1130/L85.1.

He, J., Chery, J., 2008. Slip rates of the Altyn Tagh, Kunlun and Karakorum faults (Tibet) from 3D mechanical modeling. Earth and Planetary Science Letters 274, 50–58. doi:10.1016/j.epsl.2008.06.049.

Hetzel, R., Niedermann, S., Tao, M.X., Kubik, P.W., Ivy-Ochs, S., Gao, B., Strecker, M.R., 2002. Low slip rates and long-term preservation of geomorphic features in Central Asia. Nature 417, 428–432.

Heyman, J., Stroeven, A.P., Harbor, J.M., Caffee, M.W., 2011. Too young or too old: evaluating cosmogenic exposure dating based on an analysis of compiled boulder exposure ages. Earth and Planetary Science Letters 302, 71–80. doi:10.1016/j.epsl.2010.11.040.

Imbrie, J., Hays, J.D., Martinson, D.G., McIntyre, A., Mix, A.C., Morley, J.J., Pisias, N.G., Prell, W.L., Shackleton, N.J., 1984. The orbital theory of Pleistocene climate: support from a revised chronology of the marine δ18 O record. Milankovitch and climate: understanding the response to astronomical forcing, pp. 269–305 (A. Berger, J. Imbrie, J. Hays, G. Kukla, and B. Saltzman, Reidel, Boston).

Jade, S., Bhatt, B.C., Yang, Z., Bendick, R., Gaur, V.K., Molnar, P., Anand, M.B., Kumar, D., 2004. GPS measurements from the Ladakh Himalaya, India: preliminary tests of plate-like or continuous deformation inTibet. Geological Society of America Bulletin 116, 1385–1391. doi:10.1130/B25357.1.

Jade, S., Raghavendra Rao, H.J., Vijayan, M.S.M., Gaur, V.K., Bhatt, B.C., Kumar, K., Jaganathan, S., Ananda, M.B., Dileep Kumar, P., 2010. GPS-derived deformation rates in northwestern Himalaya and Ladakh. International Journal of Earth Sciences. doi:10.1007/s00531-010-0532-3.

Jessup, M.J., Newell, D.L., Cottle, J.M., Berger, A.L., Spotilla, J.A., 2008. Orogen-parallel extension and exhumation enhanced by denudation in the trans-Himalayan Arun River gorge, Ama Drime Massif, Tibet–Nepal. Geology 36 (7), 587–590. doi:10.1130/G24722A.1.

Jolivet, J., Cattin, R., Chamot-Rooke, N., Lasserre, C., Peltzer, G., 2008. Thin-plate modeling of interseismic deformation and asymmetry across the Altyn Tagh fault zone. Geophysical Research Letters 35, L02309. doi:10.1029/2007GL031511.

Kali, E., Leloup, P.H., Arnaud, N., Maheo, G., Liu, D., Boutonnet, E., Van der Woerd, J., Liu, X., Liu-Zeng, J., Li, H., 2010. Exhumation history of the deepest central Himalayan rocks (Ama Drime range): key P–T–D–t constraints on orogenic models. Tectonics 29. doi:10.1029/2009TC002551.

Kirby, E., Harkins, N., Wang, E., Shi, X., Fan, C., Burbank, D., 2007. Slip-rate gradients along the eastern Kunlun fault. Tectonics 26. doi:10.1029/2006TC002033.

Lacassin, R., Valli, F., Arnaud, N., Leloup, P.H., Paquette, J.L., Li, H., Tapponnier, P., Chevalier, M.L., Guillot, S., Maheo, G., Zhiqin, X., 2004. Large-scale geometry, offset and kinematic evolution of the Karakorum fault, Tibet. Earth and Planetary Science Letters 219, 255–269. doi:10.1016/S0012-821X(04)00006-8.

Lal, D., 1991. Cosmic ray labeling of erosion surfaces: in situ nuclide production rates and erosion models. Earth and Planetary Science Letters 104, 424–439. doi:10.1016/0012-821X(91)90220-C.

Lal, D., Harris, N., Sharma, K., Gu, Z., Ding, L., Liu, T., Dong, W., Caffee, M.W., Jull, A., 2003. Erosion history of the Tibetan Plateau since the last interglacial: constraints from the first studies of cosmogenic ^{10}Be from Tibetan bedrock. Earth and Planetary Science Letters 217, 33–42. doi:10.1016/S0012-821X(03)00600-9.

Lasserre, C., et al., 1999. Postglacial left slip-rate and past occurrence of M ≥ 8 earthquakes on the western Haiyuan fault, Gansu, China. Journal of Geophysical Research 104 (B8), 17,633–17,651. doi:10.1029/1998JB900082.

Lasserre, C., Gaudemer, Y., Tapponnier, P., Mériaux, A.-S., Van der Woerd, J., Yuan, D., Ryerson, R.J., Caffee, M.W., 2002. Fast late Pleistocene slip rate on the Leng Long Ling segment of the Haiyuan fault, Qinghai, China. Journal of Geophysical Research 107 (B11), 2276. doi:10.1029/2000JB000060.

Li, H., Van der Woerd, J., Tapponnier, P., Klinger, Y., Xuexiang, Q., Jingsui, Y., Yintang, Z., 2005. Slip rate on the Kunlun fault at Hongshui Gou, and recurrence time of great events comparable to the 14/11/2001, Mw~7.9 Kokoxili earthquake. Earth and Planetary Science Letters 237 (1–2), 285–299. doi:10.1016/j.epsl.2005.05.041.

Lifton, N., Bieber, J., Clem, J., Duldig, M., Evenson, P., Humble, J., Pyle, R., 2005. Addressing solar modulation and long-term uncertainties in scaling secondary cosmic rays for in situ cosmogenic nuclide applications. Earth and Planetary Science Letters 239, 140–161. doi:10.1016/j.epsl.2005.07.011.

Liu, Q., 1993. Paleoclimat et contraintes chronologiques sur les mouvements recents dans l'ouest du Tibet: failles du Karakorum et de Longmu Co-Gozha Co, lacs en pull-apart de Longmu Co et de Sumxi Co, Ph.D. thesis Paris 7.

Loveless, J.P., Meade, B.J., 2011. Partitioning of localized and diffuse deformation in the Tibetan Plateau from joint inversions of geologic and geodetic observations. Earth and Planetary Science Letters 303, 11–24. doi:10.1016/j.epsl.2010.12.014.

Meade, B., 2007a. Present-day kinematics at the India–Asia collision zone. Geology 35, 81–84. doi:10.1130/G22924A.1.

Meade, B., 2007b. Present-day kinematics at the India–Asia collision zone: reply. Geology 36. doi:10.1130/G24640Y.1.

Meriaux, A.-S., Ryerson, F.J., Tapponnier, P., Van der Woerd, J., Finkel, R.C., Xiwei, Xu, Zhiqin, Xu, Caffee, M.W., 2004. Rapid slip along the central Altyn Tagh fault: morphochronologic evidence from Cherchen He and Sulamu Tagh. Journal of Geophysical Research 109 (B18). doi:10.1029/2003JB002558 (art. no. B06,401).

Meriaux, A.-S., et al., 2005. The Aksay segment of the northern Altyn Tagh fault: tectonic geomorphology, landscape evolution, and Holocene slip rate. Journal of Geophysical Research 110. doi:10.1029/2004JB003210 (Art. No. B04404).

Meyer, B., Tapponnier, P., Gaudemer, Y., Peltzer, G., Guo, S.-M., Chen, Z.-T., 1996. Rate of left-lateral movement along the easternmost segment of the Altyn Tagh Fault, east of 96 E (China). Geophysical Journal International 124, 29–44.

Murphy, M.A., Burgess, W.P., 2006. Geometry, kinematics, and landscape characteristics of an active transtension zone, Karakoram fault system, Southwest Tibet. Journal of Structural Geology 28, 268–283. doi:10.1016/j.jsg.2005.10.009.

Murphy, M.A., Copeland, P., 2005. Transtensional deformation in the Central Himalaya and its role in accommodating growth of the Himalayan orogen. Tectonics 24 (TC4012). doi:10.1029/2004TC001659.

Murphy, M.A., Yin, A., Kapp, P., Harrison, T.M., Lin, D., Guo, J.H., 2000. Southward propagation of the Karakoram fault system, southwest Tibet: timing and magnitude of slip. Geology 28, 451–454. doi:10.1130/0091-7613.

Murphy, M.A., Yin, A., Harrison, T.M., Manning, C.E., Ryerson, F.J., Lin, D., Jinghui, G., 2002. Structural evolution of the Gurla Mandhata detachment system, southwest Tibet: implications for the eastward extent of the Karakoram fault system. Geological Society of America Bulletin 144, 428–447. doi:10.1130/0016-7606(2002)114<0428:SEOTGM>2.0.CO;2.

Owen, L.A., Yi, C., Finkel, R.C., Davis, N.K., 2010. Quaternary glaciation of Gurla Mandhata (Naimon'anyi). Quaternary Science Reviews 29, 1817–1830. doi:10.1016/j.quascirev.2010.03.017.

Peltzer, G., Tapponnier, P., 1988. Formation and evolution of strike-slip faults, rifts, and basins during the India–Asia collision: an experimental approach. Journal of Geophysical Research 93, 15085–15117. doi:10.1029/JB093iB12p15085.

Peltzer, G., Tapponnier, P., Armijo, R., 1989. Magnitude of Late Quaternary left-lateral displacements along the north edge of Tibet. Science 246, 1285–1289. doi:10.1126/science.246.4935.1285.

Phillips, R.J., Searle, M.P., 2007. Macrostructural and microstructural architecture of the Karakoram fault: relationship between magmatism and strike-slip faulting. Tectonics 26. doi:10.1029/2006TC00946.

Phillips, R.J., Parrish, R.R., Searle, M.P., 2004. Age constraints on ductile deformation and long-term slip rates along the Karakoram fault Ladakh. Earth and Planetary Science Letters 226, 305–319. doi:10.1016/j.epsl.2004.07.037.

Putkonen, J., Swanson, T., 2003. Accuracy of cosmogenic ages for moraines. Quaternary Research 59, 255–261. doi:10.1016/S0033-5894(03)00006-1.

Ratschbacher, L., Frisch, W., Liu, G., 1994. Distributed deformation in southern and western Tibet during and after the India–Asia collision. Journal of Geophysical Research 99, 19917–19945.

Robinson, A.C., 2009a. Geologic offsets across the northern Karakorum fault: implications for its role and terrane correlations in the western Himalayan–Tibetan orogen. Earth and Planetary Science Letters 279, 123–130. doi:10.1016/j.epsl.2008.12.039.

Robinson, A.C., 2009b. Evidence against Quaternary slip on the northern Karakorum Fault suggests kinematic reorganization at the western end of the Himalayan–Tibetan orogen. Earth and Planetary Science Letters 286, 158–170. doi:10.1016/j.epsl.2009.06.025.

Rutter, E.H., Faulkner, D.R., Brodie, K.H., Phillips, R.J., Searle, M.P., 2007. Rock deformation processes in the Karakoram fault zone, Eastern Karakoram, Ladakh, NW India. Journal of Structural Geology 29, 1315–1326. doi:10.1016/j.jsg.2007.05.001.

Ryerson, F.J., Tapponnier, P., Finkel, R.C., Meriaux, A.S., Van der Woerd, J., Lasserre, C., Chevalier, M.L., Xiwei, X., Li, H., King, G.C.P., 2006. Applications of morphochronology to the active tectonics of Tibet. In: Siame, L.L., Bourles, D.L., Brown, E.T. (Eds.), Application of cosmogenic nuclides to the study of Earth surface processes: the practice and the potential: Geol. Soc. of Am. Special Paper, 415, pp. 61–86. doi:10.1130/2006.2415(05).

Searle, M.P., Weinberg, R.F., Dunlap, W.J., 1998. Transpressional tectonics along the Karakoram fault zone, northern Ladakh: constraints on Tibetan extrusion. In: Holdsworth, R.E. (Ed.), Continental Transpressional and Transtensional Tectonics: Geological Society of London Special Publication, 135, pp. 307–326. doi:10.1144/GSL.SP.1998.135.01.20.

Staudacher, T., Sarad, P., Tapponnier, P., Fort, M., Allegre, C., 1992. Preliminary ages of the Jiefang Qiao glacier moraines, Western Tibet, determined from cosmogenic noble gas isotopes. International Symposium on the Karakorum and Kunlun Mountains, Abstracts, Kashi, China.

Stone, J.O., 2000. Air pressure and cosmogenic isotope production. Journal of Geophysical Research 105, 23,753–23,760. doi:10.1029/2000JB900181.

Styron, R.H., Taylor, M.H., Murphy, M.A., 2011. Oblique convergence, arc-parallel extension, and the role of strike-slip faulting in the High Himalaya. Geosphere 7 (2), 582–596. doi:10.1130/GES00606.1.

Tapponnier, P., Xu, Z., Roger, F., Meyer, B., Arnaud, N., Wittlinger, G., Yang, J., 2001. Oblique stepwise rise and growth of the Tibet Plateau. Science 294 (5547), 1671–1677. doi:10.1126/science.105978.

Thatcher, W., 2007. Microplate model for the present-day deformation of Tibet. Journal of Geophysical Research 112, B01401. doi:10.1029/2005JB004244.

Thatcher, W., 2009. How the continents deform: the evidence from Tectonic Geodesy. Annual Review Earth Planetary Science 37, 237–262. doi:10.1146/annurev.earth.031208.100035.

Valli, F., Arnaud, N., Leloup, P.H., Sobel, E.R., Maheo, G., Lacassin, R., Guillot, S., Li, H., Tapponnier, P., Xu, Z., 2007. Twenty million years of continuous deformation along the Karakoram fault, western Tibet: a thermochronological analysis. Tectonics 26, TC4004. doi:10.1029/2005TC001913.

Valli, F., et al., 2008. New U–Th/Pb constraints on timing of shearing and long-term slip-rate on the Karakorum fault. Tectonics 27, TC5007. doi:10.1029/2007TC002184.

Van Der Woerd, J., Ryerson, F.J., Tapponnier, P., Gaudemer, Y., Finkel, R.C., Mériaux, A., Caffee, M.W., Guoguang, Z., Qunlu, H., 1998. Holocene left-slip rate determined by cosmogenic surface dating on the Xidatan segment of the Kunlun fault (Qinghai, China). Geology 26, 695–698. doi:10.1130/0091-7613(1998)026<0695:HLSRDB>2.3.CO;2.

Van Der Woerd, J., Ryerson, F.J., Tapponnier, P., Mériaux, A.S., Gaudemer, Y., Meyer, B., Finkel, R.C., Caffee, M.W., Guoguang, Z., Xu, Z., 2000. Uniform slip-rate along the Kunkun fault: implications for seismic behaviour and large-scale tectonics. Geophysical Research Letters 27, 2353–2356. doi:10.1029/1999GL011292.

Van Der Woerd, J., Tapponnier, P., Ryerson, F.J., Mériaux, A.S., Meyer, B., Gaudemer, Y., Finkel, R.C., Caffee, M.W., Guoguang, Z., Zhiqin, Xu., 2002. Uniform postglacial slip-rate along the central 600km of the Kunlun fault (Tibet), from ^{26}Al, ^{10}Be, and ^{14}C dating of riser offsets, and climatic origin of the regional morphology. Geophysical Journal International 148, 356–388. doi:10.1046/j.1365-246x.2002.01556.x.

Wallace, K., Yin, G.H., Bilham, R., 2004. Inescapable slow slip on the Altyn Tagh fault. Geophysical Research Letters 31 (9). doi:10.1029/2004GL019724.

Wang, Q., et al., 2001. Present-day crustal deformation in China constrained by global positioning system measurements. Science 294 (5542), 574–577. doi:10.1126/science.1063647.

Wang, S., Fang, X., Lai, Q., Zheng, D., Wang, Y., 2009. New radiometric dating constrains the time for initiation of the Karakorum fault zone (KFZ), SW Tibet. Tectonophysics 475, 503–513. doi:10.1016/j.tecto.2009.06.016.

Wang, H., Liu, M., Cao, J., Shen, X., Zhang, G., 2011. Slip rates and seismic moment deficits on major active faults in mainland China. Journal of Geophysical Research 116, B02405. doi:10.1029/2010JB007821.

Whipple, K.X., Tucker, G.E., 1999. Dynamics of the stream-power river incision model: implications for height limits of mountain ranges, landscape response timescales, and research needs. Journal of Geophysical Research 104, 17661–17674. doi:10.1029/1999JB900120.

Wright, T.J., Parsons, B., England, P.C., Fielding, E.J., 2004. InSAR observations of low slip rates on the major faults of western Tibet. Science 305 (5681), 236–239. doi:10.1126/science.1096388.

Xu, X., Tapponnier, P., et al., 2005. Late Quaternary sinistral slip rate along the Altyn Tagh fault and its structural transformation model. Science in China Series D: Earth Sciences 48, 384–397. doi:10.1360/02yd0436.

Zechar, J.D., Frankel, K.L., 2009. Incorporating and reporting uncertainties in fault slip rates. Journal of Geophysical Research 114, B12407. doi:10.1029/2009JB006325.

Zhang, P.Z., Shen, Z., Wang, M., Gan, W.J., Burgmann, R., Molnar, P., 2004. Continuous deformation of the Tibetan Plateau from global positioning system data. Geology 32, 809–812. doi:10.1130/G20554.1.

Zhang, P.Z., Molnar, P., Xu, X., 2007. Late Quaternary and present-day rates of slip along the Altyn Tagh Fault, northern margin of the Tibetan Plateau. Tectonics 26. doi:10.1029/2006TC002014.